Horizon 2020 Programme

METIS

Research and Innovation Action (RIA)

This project has received funding from the European Union's Horizon 2020 research and innovation programme under grant agreement No 945121

Start date : 2020-09-01 Duration : 48 Months

Methodology for site response analysis to obtain surface ground motions from hazard consistent rock motions

Authors : Dr. Irmela ZENTNER (EDF), Michail Korres (EDF), Vinicius Alves-Fernandes (EDF), Irmela Zentner, (EDF), Marco Pilz (GFZ)

METIS - Contract Number: 945121

Project officer: Katerina PTACKOVA

Document title	Methodology for site response analysis to obtain surface ground motions from hazard consistent rock motions
Author(s)	Dr. Irmela ZENTNER, Michail Korres (EDF), Vinicius Alves-Fernandes (EDF), Irmela Zentner, (EDF), Marco Pilz (GFZ)
Number of pages	48
Document type	Deliverable
Work Package	WP5
Document number	D5.3
Issued by	EDF
Date of completion	2024-01-15 19:21:30
Dissemination level	Public

Summary

The METIS project has the goal to improve the overall methodology for seismic risk assessment of nuclear power plants subject to seismic load. This includes seismic hazard, fragility, and system assessment. The strategy developed in METIS project is to develop seismic hazard on rock conditions. The impact of the surrounding soil and site conditions is then considered as part of the structural analysis where the structure is considered within its local environment. This approach allows for detailed site response in the framework of graduated approach. It also has the advantages that it allows developing site response only for the scenarios of interest for the engineer. This means that this strategy requires much less analysis than what would be required for introducing detailed site response in hazard curves and avoids double counting of related uncertainties. This reports first provides possible criteria to decide the kind of site response analyse adequate for a given site and then introduces different possible approaches to model 1D, 2D and 3D site response. While the 1D site response analysis has been widely studied and applied in literature, including for nuclear safety applications, the 2D and in particular 3D site response analysis are still challenging in terms of modelling, data and computational resources. The strategies discussed in this work to tackle the multi-dimensional (2D and 3D site effects) analysis in a FEM framework are plane wave excitation with the Free-Field Boundary Condition in a FEM framework and the Domain Reduction Method for the definition of a complex 3D input motion at the boundaries of the FE model. The application of the site response strategies to METIS cases study will be reported in the dedicated deliverable, D5.4.

Approval

Date	By
2024-01-30 13:56:06	Mrs. Paolo BAZZURRO (IUSS)
2024-01-30 14:04:52	Dr. Irmela ZENTNER (EDF)

METIS

Seismic Risk Assessment for Nuclear Safety

Research & Innovation Action

NFRP-2019-2020

Methodology for site response analysis to obtain surface ground motions from hazard consistent rock motions

Deliverable D5.3

Version N°1

Authors:

Michail Korres, Vinicius Alves-Fernandes, Irmela Zentner (EDF),

Marco Pilz (GFZ)

This project has received funding from the Horizon 2020 programme under grant agreement n°945121. The content of this presentation reflects only the author's view. The European Commission is not responsible for any use that may be made of the information it contains.

Disclaimer

The content of this deliverable reflects only the author's view. The European Commission is not responsible for any use that may be made of the information it contains.

Document Information

Grant agreement	945121
Project title	Methods And Tools Innovations For Seismic Risk Assessment
Project acronym	METIS
Project coordinator	Dr. Irmela Zentner, EDF
Project duration	1st September 2020 – 31st August 2024 (48 months)
Related work package	WP5 - Ground motion selection for engineering analyses, including site response
Related task(s)	Task 5.3 - Site response modelling to obtain surface ground motions from rock-hazard consistent ground motions
Lead organisation	EDF
Contributing partner(s)	EDF, GFZ, UL

History

Version	Submitted by	Reviewed by	Date	Comments
N°1	Michail Korres	Stefano Parolai	22/11/2023	Focus on section 2
		Charisis Chatzigogos	27/11/202	
		Tadeusz.Szczesiak Rainer Zinn Peter Rangelow, Peter Zwicky	27/11/2023	Focus on section 3,4
	Irmela Zentner		4/01/2024	Report updated

Table of Contents

Abbreviations and Acronyms

Acronym	Description
WP	Work Package
DRM	Domain Reduction Method
EQL	Equivalent Linear
FFBC	Free Field Boundary Condition
GMTH	Ground Motion Time history
GMM	Ground Motion Model
HPC	High Performance Computing
PSHA	Probabilistic Seismic Hazard Assessment
SSI	Soil Structure Interaction
STD	Standard deviation

Summary

The METIS project has the goal to improve the overall methodology for seismic risk assessment of nuclear power plants subject to seismic load. This includes seismic hazard, fragility, and system assessment. The strategy developed in METIS project is to develop seismic hazard on rock conditions. The impact of the surrounding soil and site conditions is then considered as part of the structural analysis where the structure is considered within its local environment. This approach allows for detailed site response in the framework of graduated approach. It also has the advantages that it allows developing site response only for the scenarios of interest for the engineer. This means that this strategy requires much less analysis than what would be required for introducing detailed site response in hazard curves and avoids double counting of related uncertainties. This reports first provides possible criteria to decide the kind of site response analyse adequate for a given site and then introduces different possible approaches to model 1D, 2D and 3D site response.

The application of the site response strategies to METIS cases study will be reported in the dedicated deliverable, D5.4.

Keywords

Site response, nonlinear, equivalent linear, 1D, 2D 3D, soil column, ground motion, rock, soil, uncertainty, response spectra

1. Introduction

The METIS project has the goal to improve the overall methodology for seismic risk assessment of nuclear power plants subject to seismic load. This includes seismic hazard, fragility, and system assessment. The strategy developed in METIS project is to develop seismic hazard on rock conditions. The impact of the surrounding soil and site conditions is then considered as part of the structural analysis where the structure is considered within its local environment. This approach allows for detailed site response in the framework of graduated approach. It also has the advantages that it allows developing site response only for the scenarios of interest for the engineer. This means that this strategy requires much less analysis than what would be required for introducing detailed site response in hazard curves. Also, this approach fully integrates physics-based site response analysis in the risk assessment analysis chain.

In the current nuclear practice and most regulations seismic hazard is defined at the free-field (stars 1 and 2, respectively for soil and rock condition) where site response is accounted for in a simplified way through GMM and then again modelled with more detail in the structural response and SSI modelling step. The latter generally implies double counting and possibly bias due to conservative assumptions at the interface between hazard and structural response. This can be overcome by developing a unified approach where seismic hazard is defined on rock and bedrock conditions while site response is introduced in the structural modelling step.

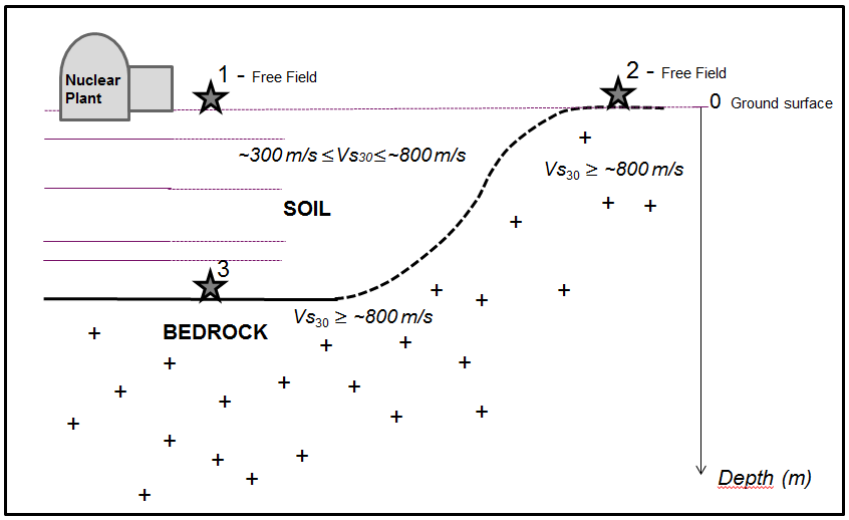

Figure 1. Schematic view of the site configuration and the definition of the « reference or control point » on bedrock (3) and free field (1,2). Figure from (Berge-Thierry, et al., 2017).

Indeed, the strategy adopted here prevents from dealing with inconsistencies in the site response conducted for hazard and the site modelling required for Soil Structure Interaction (SSI) analysis.

In consequence it avoids double counting of uncertainties related to site response and hazard which is a well-known issue in seismic assessments. It is compatible with a wider range of approaches for site response analysis. It allows for more detailed site response modelling, spanning from nonlinear 1D to 2D or 3D, than what is possible when introducing site response in the hazard analysis. The approach presented here is flexible and can accommodate more detailed site response analysis. Interestingly, it is fully in line with findings from SINAPS@ project (Berge-Thierry, et al., 2017) and the findings of (Laurendeau, et al., 2017) where a control point at the bedrock level and elaboration of specific GMM for rock site condition is proposed. In addition, rock ground motion models for the computation of hazard on rock and bedrock conditions are becoming more and more common and well defined. For

example, in (Shible, Hollender, Traversa, & Bard, 2023), the authors develop ground motion for rock sites from deconvolved ground-motion models using site response from generalized inversion techniques.

In what follows we provide possible criteria to decide the kind of site response analysis adequate for a given site and then introduce different possible approaches to model 1D, 2D and 3D site response.

The application of the site response strategies to METIS case study will be reported in the dedicated deliverable, D5.4.

2. Criteria for the identification of 1D/2D or 3D site response

A first step consists in the definition of criteria that allow to decide whether 1D or multidimensional site response analysis are required for the site under study. This depends on the configuration of the site, such as only horizontal stratification of the soil or the presence of prominent geological features such as a basin, layer folding, or extended fault configurations that can have a major impact on the incoming wave field. A quantitative description of the limits of the 1D assumption and a clear estimation of the possible impact of 2D and 3D effects, however, remains a difficult task. While many numerical studies have focused on simulations in idealized 2D basins with well-known shapes of the sediment-bedrock interface and idealized topographies, only a small number of studies (e.g., (Thompson E. M., Baise, Tanaka, & Kayen, 2012; Laurendeau, et al., 2017)) have tried to evaluate the validity of the 1D assumption and identify the different levels of complexity of site response that should be accounted for.

Here, strategies to assess the validity of the 1D assumption and to investigate the ability to identify 2D and 3D site effects are proposed:

- using earthquake-based criteria when seismic records but no site-specific information is available
- and using transfer function variability when additional site-specific information is available.

This is described with more detail in what follows.

2.1. Single-station earthquake-based criteria if no site-specific information is available

2.1.1. Methodology

When looking at single-station recordings in complex environments, it has often been observed that the spectra of the two horizontal components are different in shape and amplitude. 2D/3D effects had often been cited as the cause though with different impacts of these effects on these two measures (Uebayashi H. , 2003; Roten, Fäh, Cornou, & Giardini, 2006; Barnaba, et al., 2010; Uebayashi, Kawabe, & Kamae, 2012; Matsushima, Kosaka, & Kawase, 2017). The visibility of such site-specific 2D/3D effects on the horizontal component is frequency-dependent: the maximum amplification is generally expected to occur for frequencies at which the incident wave-length is comparable to the length and/or width of the morphological relief (corresponding to the longitudinal or transverse profile in a bi-dimensional resonance case). Since 2D/3D effects generally involve different kinds of seismic waves (e.g., diffracted body and surface waves in areas characterized by strong lateral variations of the thickness of the sedimentary cover) and since these effects might show up during different times of the wave window, a simple time-window scheme will hamper a proper identification. Therefore, we will analyse these effects in the spectral domain accounting for differences both in spectral shape and amplitude.

Three different measures are applied to assess the occurrence of 2D/3D site effects, namely differences in amplitude, differences in spectral shape and the within-site variability. For measuring the differences in amplitude between the horizontal components, i.e. measuring how far apart are the two horizontal components, we have relied on the normalized divergence distance d (Sjovold 1977)

$$d = \frac{1}{N}\sum_{f_1}^{f_2}\frac{(NS(f)-EW(f))^2}{(NS(f)+EW(f))^2} \tag{1.1}$$

Herein, the squared difference at each frequency value f is used for the calculation of the total distance, i.e. this definition follows the L2 norm and is based on the Euclidean distance between the horizontal components. Compared to other Euclidean distance measures, for peaked data (i.e. amplification peaks in the horizontal spectra), d outperforms other groups of measures in terms of its discriminating power (Abu Alfeilat et al. 2019). In Equation (1.1), f1 and f2 define the frequency range over which the comparison is carried out using N spectral values. NS and EW describe the frequency-dependent horizontal Fourier amplitude spectra (FAS). Each term in the summation is squared, from which it follows that the relationship directly assesses any differences in amplitude. From a theoretical point of view, d takes values between zero and one, being zero if (and only if) the two components are identical.

Complementarily, we have selected the Jensen Shannon difference J from the Shannon entropy family to compare the shapes of the two spectra,

$$J = \frac{1}{2}\left(\sum_{f_1}^{f_2}\left(NS(f)\ln\left(\frac{2NS(f)}{NS(f)+EW(f)}\right)\right)+\sum_{f_1}^{f_2}\left(EW(f)\ln\left(\frac{2EW(f)}{NS(f)+EW(f)}\right)\right)\right) \tag{1.2}$$

J describes the mean relative entropy between the variation of the two horizontal spectra and their respective mean (Lin, 1991). Herein, entropy refers to the degree of disorder (or randomness) in a situation. It quantifies how distinguishable the shapes of the two spectra are from each other. It is equal to zero only if the two components are indistinguishable, i.e. identical.

For each study site - besides the two parameters mentioned above - we have further investigated the inter-event variability of the H/V spectral ratios as a third criterion. The same measure has already been proposed by (Thompson E. M., Baise, Tanaka, & Kayen, 2012) using surface-to-borehole spectral ratios although it has recently been shown that surface-to-borehole spectral ratios have a limited usable frequency range with respect to H/V spectral ratios (Zhu, et al., 2021). If a large H/V inter-event variability is observed at a single site, such differences could be caused by event-specific site effects linked to source-site configurations. This includes (1) the variability in source azimuth, incidence angle and wave field on the input motion in which, for example, shallow events might generate local surface waves which can contribute to azimuthal-dependent amplification in certain frequency bands, (2) the lateral variability of the site (i.e. surface and subsurface topography), and (3) temporally variable nature of soil properties due to soil nonlinearity and/or climatic factors (Alshembari, et al., 2019). With various degrees all these effects will negatively influence the ability for 1D ground-motion modelling at this site but all of them will contribute to a large within-site variability.

Once the three individual parameters are available, they have been normalized separately. For every parameter, we subtract the respective parameter mean and divide the results by the standard deviation to shift each distribution to have a mean of zero and a standard deviation of one. Then, the three standardized parameters are summed, providing an index I which assumes a value in the range 0 to 1 with 0 indicating a fully 1D behaviour while an index of 1 represents the certainty of significant horizontal variability at this site.

2.1.2. Example application and comparison with previous studies

We have used earthquake recordings from the KiK-net strong-motion network since, due to the previously published studies, this always a comparison and a validation of the results. The selected

ground-motions are a subset of the recordings compiled and processed by (Bahrampouri, Rodriguez-Marek, & Bommer, 2019) who collected the strong motion data for earthquakes with magnitude larger than 3 which occurred between 1996 and 2017 . In addition, we choose only earthquakes with at least three usable recordings for which, in a first step, the peak ground acceleration (PGA) has to be less than 0.1 g for keeping the analysis in the linear range.

For the analysed 689 network sites for the entire KiK-net, Figure 1 plots the distribution of the three site parameters and the final value of I. The parameter d and the standard deviation approximately follow a normal distribution while for J and correspondingly for the final index I the distributions are slightly skewed with a tendency towards smaller values.

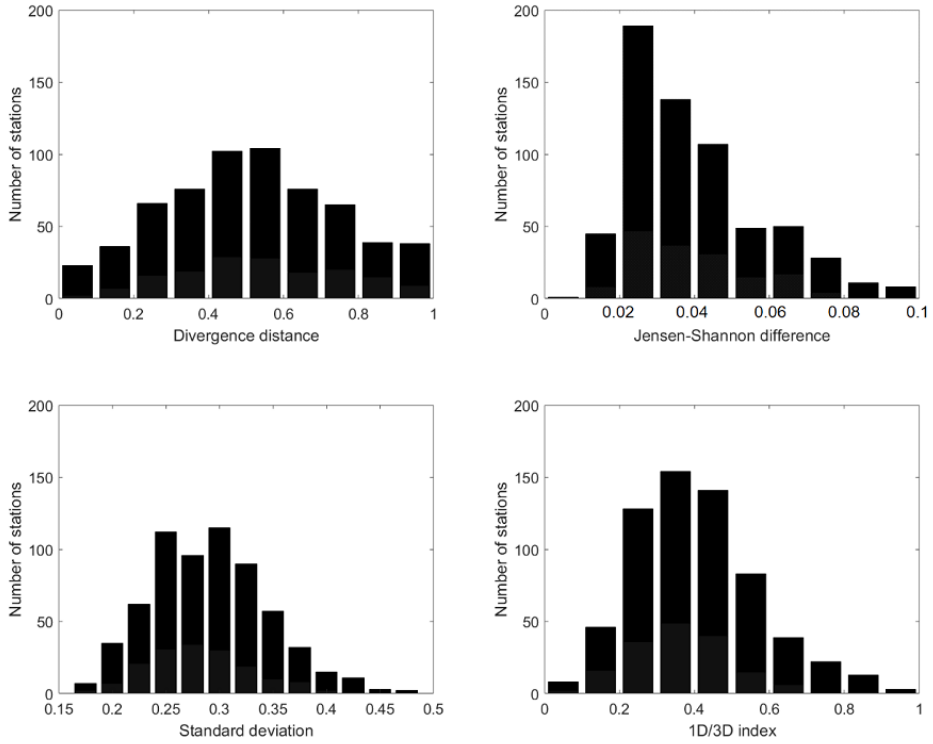

Figure 2: Quantitative distribution of the number of stations for d (top left), J (top right), standard deviation (bottom left) and final index (bottom right) for 689 analysed KiK-net sites.

While there is only a limited number of sites with extreme values for I (for example, there 54 sites with $I \leq 0.2$ and 16 sites with $I \geq 0.8$ although these thresholds are only set as a tendency), most sites (almost 90 %) cannot be characterized as purely 1D or purely 2D/3D. However, for grouping sites as 1D or 2D/3D sites, we refrain from using strict threshold values since this would mean that such classification would be depending on our choices. On the contrary, the use of an index quantifying the probability that a site is affected by 2D/3D effects offers the possibility to set user- and application-specific confidence levels.

To be able to better classify the results, we compared the results with findings of previous studies. (Tao & Rathje, 2020) recently presented a taxonomy to assess the suitability of 1D analysis considering the justification of peaks in the H/V spectral ratio and the presence of true and pseudo resonances at a site. For minimizing any parametric uncertainty in their modelling approach, (Tao & Rathje, 2020) re-inverted the available velocity profiles at some KiK-net sites. For 28 studied KiK-net sites, 21 are classified by (Tao & Rathje, 2020) to be modelled well by 1D analysis. Based on this study, the corresponding list of 1D sites takes a mean of $I = 0.40 \pm 0.16$ and 18 of these 21 sites are characterized by I of less than 0.5. Also for the seven non-1D sites of (Tao & Rathje, 2020), a consistent result is found: I takes much higher values with a mean of $I = 0.52 \pm 0.08$.

(Thompson E. M., Baise, Tanaka, & Kayen, 2012) have presented another thorough approach for developing a taxonomy to identify sites that can be modelled well by 1D analysis. Based on their study, 16 of 100 sites have been classified as LG (Low inter-event variability and good match between the empirical and theoretical transfer function), i.e. sites ideal for validation of 1D constitutive models. Also in our study, most of these sites show a very low value of I ($I < 0.3$) while only for a few sites significant differences occur, meaning that for these sites I takes values larger or much larger than 0.5. Here the difference is mainly caused by a significantly higher inter-event variability for the corresponding sites in this study as rather large values for the standard deviation for the corresponding sites are found. A visual inspection, however, indicates the correctness of the large standard deviation for the modelled sites.

A large number (53 of 100 studied sites) have been characterized as LP sites (Low inter-event variability and Poor level of match between the empirical and theoretical transfer function) by Thompson et al (2012). For these sites, however, it mostly takes values of less than 0.5, i.e. tending towards 1D, with a mean of 0.42 ± 0.15. As noted by (Tao & Rathje, 2019), correlation coefficients are particularly sensitive to the modelled level of damping. In turn, this might have caused a site not being considered as 1D due to a poor fit between the empirical and theoretical transfer function. This means that in this situation the underlying evaluation of the goodness-of-fit might not only be affected by the modelling uncertainty (e.g., 2D/3D effects, complex incident wave fields) but also by the parametric uncertainty of the parameters entering in the ground-motion model.

Table 1: Assignments of this study in comparison with the findings of (Thompson E. M., Baise, Tanaka, & Kayen, 2012) and (Tao & Rathje, 2020)

	Number of sites	Mainly 1D	Approach
This study	689	54	Only single station recordings required
Tao and Rathje	34	23	Re-assessment of available velocity profile for identification of pseudo-resonances
Thompson et al.	100	16	Comparison of theoretical and empirical 1D transfer function

The proposed probabilistic indexing scheme can be used to identify sites which are more likely to be affected by 2D/3D site effects indicating that more complex ground-motion modelling is required. The scheme is based on single-station earthquake recordings at surface stations only. The advantage of the presented approach that no additional site-specific information, i.e. velocity/damping profiles nor recordings at nearby reference sites are required. Although we have developed the method solely using strong-motion data from Japan, the approach is not regional-specific and could be applied to other regions with strong-motion networks and recordings like the METIS case study.

2.2. Transfer function variability if site-specific information is available.

2.2.1. Methodology

When additional information on the P- and S-wave velocity profiles is available, these data can be used to calculate empirical amplification functions and to compare the theoretical results with real-world data. This is the case for KiK net. Since interferences of up and down-going waves may lead to destructive interferences at depth, we refrain from directly calculating surface-to-downhole spectral ratios for each network site. In contrast, empirical amplification functions are calculated following the inversion procedure presented by (Edwards, Michel, Poggi, & Fah, 2013). For each recorded event, we apply a baseline correction of the strong motion time histories. Events with PGA larger than 0.1 g are excluded to keep only linear recordings. The P wave and S wave arrivals and the signal end (end of coda waves) are automatically picked up. The algorithm used for automatic selection is based on the calculation of the ratio of the Long-Term Average (LTA) over the Short-Term Average (STA). It continuously calculates the average values of the absolute amplitude of the waveform signal in two consecutive moving-time windows. To identify well the local events, we choose an LTA of 5 s, an STA of 1 s, and threshold of 0.5. If no S wave arrivals were available, a P-to-S ratio of 1.73 is used to define the start of the S wave window. The analyzed window comprises the 5% to 95% energy integral around the S wave and the coda. Unfortunately, there exists a trade-off between signal isolation and signal-to-noise ratio maximization with the robustness of low-frequency estimation, but it will less affect the high-frequency spectrum. After integration of the strong motion data to velocity, the corresponding Fourier velocity spectrum Ωij observed at station j is modelled by

$$\Omega_{ij}(f,r) = 2\pi f\, E_i(f, M_{0i}, f_{ci})\, B_{ij}\left(f, t^*_{ij}\right) S_{ij}(r, r_{0\ldots n-1}, \lambda_{1\ldots n})\, T_j(f, A_j, \kappa_j) \quad (1.3)$$

in which f is the frequency, r is the hypocentral distance, Ei (f,M0i,fci) is the source model, Bij (f, tij*) is the intrinsic attenuation along the ray path with attenuation parameter t* (following (Anderson & Hough, 1984)), Sij (r,r0…n-1,λ1…n) is the frequency-independent amplitude decay with distance (geometrical spreading), and Tj (f,Aj,κj) is the site response function at station j. The source spectrum Ei is considered to be a (Brune, 1970) ω²-spectrum with an event-specific corner frequency fc and a long-period spectral plateau defined by the seismic moment M0i. (Oth, Bindi, Parolai, & Giacomo, 2010) showed that for KiK-net data the source spectra can be well explained using the ω2-model. The geometric spreading function Sij is described as a decay function with a constant, frequency-independent exponential decay in the form r –λ. An initial spherical decay, i.e. λ = 1.0, is followed by attenuation slightly lower than spherical with λ = 0.9 for r > 150 km (trapped surface wave (cylindrical) spreading, Kawase 2006).

The local site response can then be modeled as

$$T_j(f, A_j, \kappa_j) = A_j a_j(f) e^{-\pi f \kappa_j} \quad (1.4)$$

in which Aj is the average site response relative to a given regional reference (Poggi et al. 2013), aj(f) is the normalized frequency dependent elastic site response function and κj is the relative site dependent local attenuation parameter with respect to the local site-specific attenuation at the reference site.

A nonlinear, two stage regression is used to separate the different contributions of equation (1) for obtaining Tj (f,Aj,κj). We first determine the combined path and site attenuation (tij* + κj) at each site, the event-common source corner frequency fc, and a spectral amplitude parameter termed the signal moment for each spectrum. A regional attenuation model is not used to predetermine tij* + κj because this requires simultaneous inversion of the full dataset (rather than the event-by-event application) and might bias the results due to model simplification. The misfit of the spectral model to the data is minimized in the log-log space using the L2 least-squares norm. Using the resulting minimum misfit

model, the residuals are then assumed to be an estimate of the normalized frequency dependent elastic component of the site function aj(f). While clearly a trade-off exists between the moment and average amplification. In order to decouple the site effect from the magnitude determination, magnitude values determined by the Japan Meteorological Agency taken from the F-net catalogue are fixed when available.

Since downhole logging has been shown to be not fully reliable for some KiK-net sites (Kawase & Matsuo, 2004, Wu et al. 2017), we need to define quantitative criteria to distinguish sites with properly resolved velocity profiles from others, so that further analyses are not biased by unreliable velocity profiles. For downhole sensors located close to or below the deepest impedance contrast, the reliability of the provided velocity profiles can be assessed based on on the comparison of the empirical and modelled fundamental resonance frequencies. The former can directly be estimated from the amplification function and the latter can be quantified by indirect modelling of the SH wave transfer function using the given velocity profiles and a correction for the reference rock. 2D/3D effects like basin-edge induced surface waves, which are accounted for in the empirical function but not in the modelled one, do not affect the fundamental frequency (e.g., (Cornou, 2003)). To compute the theoretical SH wave transfer function for vertically propagation waves, we follow the Knopoff layer-matrix formulation (Knopoff, 1964). Since no information about density is available from the logging profiles, we rely on proposed dependencies between density and P wave velocity, $\rho=0.31\ vP^{0.25}$ (Gardner & Knopoff, 1974).
We define a sufficient match between the empirical amplification function and the modelled transfer function if the ratio between the measured and the calculated fundamental resonance frequency is between 0.5 and 2 following, e.g., Cadet et al. (2012) and Wang et al. (2018) and if the correlation coefficients between the flanks of the two functions around the fundamental resonance frequency are higher than 0.5.
Although such assumptions do not rule out sites for which amplification occurs over a broad frequency band due to strong lateral variations at depth and non-horizontal layering, this criterion could be fulfilled for 287 sites of the analysed 689 sites. When this criterion was not satisfied, we follow Cadet et al. (2012) and apply the same matching condition which has been used for the fundamental resonance frequency also for the first higher mode of the theoretical SH transfer function. In addition to the 287 sites described above, this criterion was fulfilled for another 67 sites. Since the position and the amplitude of the fundamental resonance frequency is mainly controlled by the deepest impedance contrast, the second condition was established because of the non-negligible likelihood that the fundamental peak in the empirical amplification function is rejected due to a relatively low amplitude with respect to its standard deviation while for the modelled transfer function the first peak usually has significantly higher values due to pure interferences in case of vertical incidence, and is thus less likely to be rejected. From the whole dataset of 689 sites, 354 sites (51%) were found to have reliable velocity profiles and were kept for further analysis.

2.2.2. Example Application to KiK Net

Figure 2 presents a comparison of measured and modelled amplification functions. While for sites HDKH01 and YMGH17 the theoretical transfer function matches well the empirical data both in terms of resonance frequencies and amplitudes, for sites HRSH07 and IBUH06 significant differences in amplitude and shape can be found for frequencies higher than the site's fundamental frequency. However, for sites HRSH07 and IBUH06 an increasing number of peaks is observed in the high-frequency range. Such wiggles are due to the dispersive nature of basin-edge induced Rayleigh waves and have already been observed in numerical studies (Narayan & Kumar, 2013).

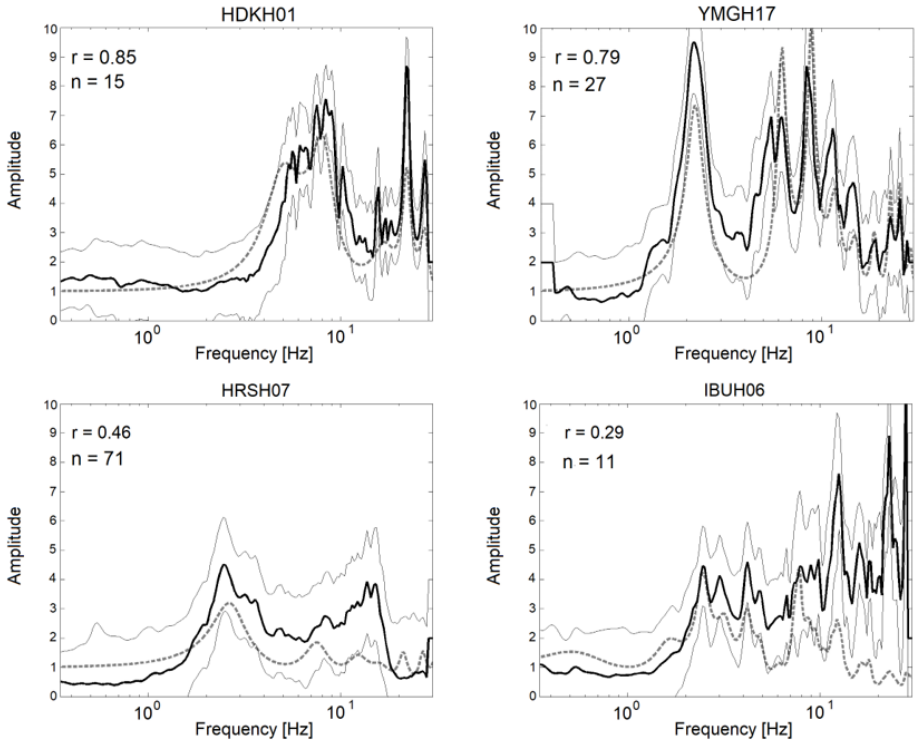

Figure 3: Theoretical 1D SH transfer function for four KiK-net sites (gray dotted lines). The black lines represent the average measured empirical amplification function plus/minus one standard deviation. HDKH01 and YMGH07 (top) are representative sites for which the 1D transfer function accurately predicts the empirical transfer function. For sites HRSH07 and IBUH06 (bottom), a significant mismatch between both amplification functions for frequencies higher than the fundamental frequency is found. r represents Spearman's rank-order correlation coefficient. n indicates the number of records used to derive the empirical amplification functions.

Similar to (Thompson E. M., Baise, Tanaka, & Kayen, 2012) we establish a quantitative criterion for the match of the two amplification functions. To this regard, we calculate Spearman's rank-order correlation coefficient r (Spearman, 1904) on logarithmically spaced samples to ensure a constant number of points at low and high frequencies. The calculation is carried out in a frequency range between the site's fundamental frequency and 25 Hz. The amplification functions at frequencies below the fundamental one usually show a gradual monotonic increase in amplitude which does not affect r. We consider potential trade-offs in the spectral inversion between elastic amplification and anelastic attenuation that may lead to incorrect amplification levels at high frequencies by using the Spearman correlation coefficient which does not care about the exact amplitude value but about comparing the shape of the two curves.

Based on a first visual inspection between the measured and modelled transfer functions and estimates of the confidence interval for Spearman's correlation coefficient for a sample data set of 354 sites, we define a threshold of $r > 0.6$ to classify sites as 1D. The classification is objectively assessed based on the comparison of the shape of the empirical amplification function for frequencies higher than f0. Of the 354 remaining sites in our database with reliable velocity profiles, 196 are classified as strictly 1D, whereas 158 sites (45%) do not fulfil these criteria and are classified as sites exhibiting 2D/3D effects. As can be seen in **Figure 4**, there is a similar number of stations in each bin for small values of r whereas the number starts to increase for $r > 0.5$. Changing the threshold of $r = 0.6$ for classifying stations as 1D and 2D/3D will slightly modify the number of sites in each class but it will not affect the results of this study substantially.

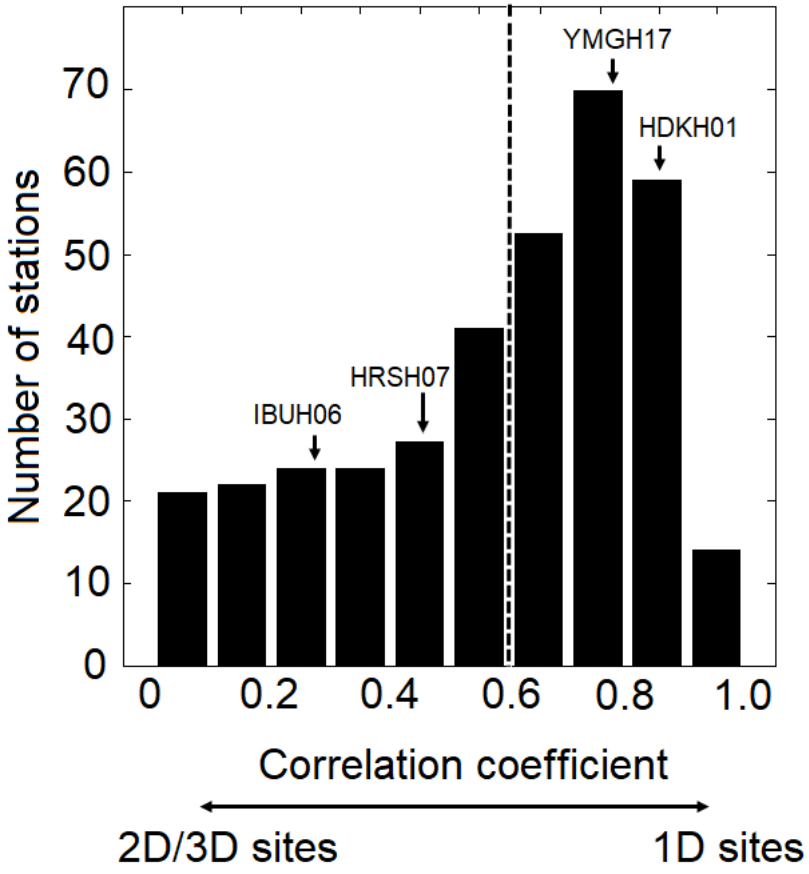

Figure 4: Classification scheme for 1D and 2D/3D sites according to Spearman's correlation coefficient. The arrows indicate r for the four representative sites shown in **Figure 3**.

In summary, given the availability of velocity profiles and based on statistical analysis and a quantitative comparison of the shapes of the empirical amplification function and the modelled 1D SH transfer function, 45% of the 354 sites in our database of KiK-net sites with reliable velocity profiles can be classified as sites exhibiting 2D/3D effects in line with the results presented in section **2.1.2.** Only a limited number of proxies like topography, bedrock shape etc. might be used to assess the general occurrence of 2D/3D effects for a large data set as a whole (details can be found in (Pilz & Cotton, 2019). The corresponding tests have been applied to the KiK-net sites as a whole. These sites are generally located on stiffer soils but inside sedimentary basins, see Aoi et al. 2004 for a further outline. For shallow valleys/basins with corresponding near-surface impedance contrasts, 2D/3D effects only affect sites close to the basin edge). Only minor inconsistencies appeared when comparing the 2D/3D spectra with the proposed EC8 spectrum shapes (**Figure 5**).

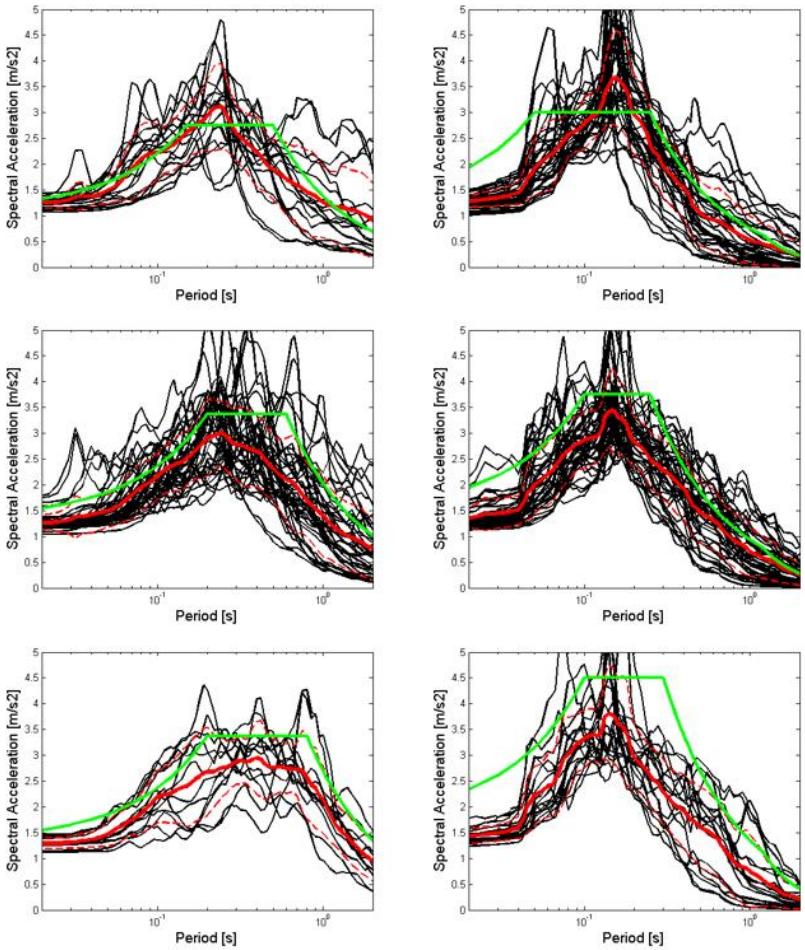

Figure 5: Elastic acceleration response spectra (ξ = 5%) scaled for PGA for 2D/3D sites for Type 1 (left) and Type 2 (right) seismicity for EC8 soil classes B (top), C (middle) and D (bottom). The red line corresponds to median empirical spectra plus/minus one standard deviation. The green line represents the EC8 proposed spectra.

This is not surprising since the EC8 spectra were calibrated on empirical data and not on 1D simulations. While for the average of the sites in the various site classes the differences in the spectral shapes between the generic and calculated spectra are minor, for single sites and/or events the differences can, however, still be large. For sites with limited site-specific information, a generic safety factor might be applied due to the larger single-station variability for 2D/3D sites. We would like to emphasize that the presented approach is not attempting to understand the physical basis of 2D/3D effects (several other papers have already discussed these effects), while the main goal was extracting the average consequences of 2D/3D effects on ground motion modelling. Such efforts do not necessarily negate further work for obtaining better predictions by using more sophisticated physical models. The results, however, in agreement with (Thompson E. M., Baise, Tanaka, & Kayen, 2012) and the results described in **section 2.1**, confirm the limits of the 1D assumption and the need to take into account 2D/3D effects.

3. Approaches for equivalent linear and nonlinear 1D ground response analysis.

In this section we describe and assess an approach that allows for the consideration of uncertainty, variability and attenuation in equivalent linear (EQL) and nonlinear 1D site response. General guidelines for standard practice of 1D ground response analysis is given in (Stewart, Afshari, & Hashash, 2014). We assess uncertainty quantification and propagation approaches and sensitivity analysis to develop best practice from standard practice to define a reduced set of 1D columns that would: (i) well represent the mean and standard deviation of soil surface ground motion variability and (ii) be easily implemented for soil-structure interaction studies as the framework of the METIS project is oriented in integrating site effects in structure's response analysis.

Here, both the variability of input ground motion on rock as well as the uncertainty related to site data are considered and propagated.

3.1. Brief literature review and state of the art

The prediction of the one-dimensional (1D) seismic site response consists of vertically propagating seismic shear waves through horizontally layered and laterally infinite homogeneous soil until the soil surface.

Obviously, despite increasing effort in site characterization, the soil conditions and the parameters governing the seismic wave propagation are not perfectly known. Therefore, it is paramount to carefully assess and propagate uncertainties in the framework of the 1D soil columns analysis.

Numerous studies examined the impact of uncertainties related to the site effects on soil surface ground motion (among others, (Thompson E. M., Baise, Kayen, & Guzina, 2009; Li & Assimaki, 2010; Pagliaroli, Lanzo, Tommasi, & Fiore, 2013; Parolai, Bindi, & Pilz, 2015; Pilz & Fäh, 2017; Tao & Rathje, 2019; El Haber, 2018; Tchawe, Gelis, BONILLA, & Lopez-Caballero, 2021) (de la Torre, Bradley, & McGann, 2021; Hallo, Bergamo, & Fäh, 2022).

Despite many advances and increased knowledge, recent studies still show discrepancies between the observed and the predicted site response (Thompson E. M., Baise, Kayen, & Guzina, 2009; Zalachoris & Rathje, 2015; Kaklamanos, Bradley, Moolacattu, & Picard, 2020). It is under study whether part of the phenomena not explicitly represented by the standard 1D analysis such as non-vertical wave incidence, small scale wave scattering and basin effects could improve predictions e.g. (Cherubini S., 2020; Youssef, 2023).

The (Toro G. R., 1995) model was extensively used in the past (Li & Assimaki, 2010; Rathje, Kottke, & Trent, 2010; Rodriguez-Marek, Rathje, Bommer, Scherbaum, & Stafford, 2014) and many others). The author used an extensive VS database to construct generic and site-specific VS randomization models, provided a generic site classification and a base case VS profile in order to study the impact of soil profile uncertainty on the site response.

However, this approach is not perfectly suited for best-estimate and site-specific applications, in particular when borehole and geophysical site data is available. Also, as pointed out in recent work, it does not necessarily guarantee the experimental site signatures in terms of surface-wave dispersion curves and fundamental resonance frequency (f0) to be replicated, as recently investigated (Griffiths et al., 2016; Youssef et al 2023). In consequence in such cases, it can lead to excessive variability of shear wave velocity profiles and an overestimation of the expected variability in site response estimates (Teague et al., 2018; Kaklamanos et al., 2020 Passeri et al. 2020).

3.2. Modeling soil behavior by equivalent linear and nonlinear approaches

Equivalent linear (EQL) approach is based on an iterative procedure of linear elastic simulations in frequency domain, for which soil dynamic properties (shear modulus and hysteretic damping) is updated at each iteration and for each soil layer based on the 65% of the maximum shear strain obtained during the shaking (this value may depend also on earthquake magnitude (Idriss, Sun, University of California, Building, & Division, 1992), although 65% remains the reference value in the literature). The procedure stops when relative difference of soil shear modulus at the different layers between 2 iterations is lower than a threshold value (e.g. 5%). The procedure was first developed by (Idriss, Seed, Mechanics, & Laboratory, 1967) and since then it has been widely used both by researchers and industry as it has been acknowledged to well capture soil nonlinear behaviour during shaking for low-to-moderate strains, for which soil dilatancy does not yet play a major role on the soil behaviour. This approach is implemented in code_aster software (`DEFI_SOL_EQUI` operator - R4.05.06), based on a finite element discretisation of the soil column and a dynamic linear solver in frequency domain. Refinements from the standard procedure have been proposed by authors and have been implemented in code_aster: (i) considering simultaneously 2 horizontal components for soil column modelling and (ii) considering pore pressure build-up by simplified Byrne model as proposed by (Kteich, Labbé, Javelaud, Semblat, & Bennabi, 2019).

Soil nonlinear models are generally classified in two main types: total or effective stress models. Total stress models are more generally used for ground response analysis, as effective stress approach is essentially deployed when pore-pressure build-up cannot be excluded during shaking and liquefaction analysis have to be performed, which is more often the case on the analysis of geotechnical structures (dams, …). In this sense, many total stress nonlinear models are directly written for soils shear response only, which simplifies both its numerical implementation and calibration. Nevertheless, on both cases ground response analysis is based on the dynamic response of a finite element model of the soil column solved in time domain.

One important factor of discrepancy between EQL and nonlinear models is how damping is modelled. Indeed, EQL approach considers hysteretic frequency-independent damping, as the model is solved in frequency domain. Nonlinear models, however, have to be solved in time-domain, and in this case different sources of damping have to be accounted for and calibrated:

- Material hysteretic damping, coming from kinematic hardening for 3D soil models or Masing's rules for shear behaviour implementation only, but which overestimates damping at high shear strains. Authors have worked in proposing models to better account for high strain damping and maximum shear stress (Groholski, et al., 2016),

- Viscous damping, which may be implement by Rayleigh coefficients and can be used to take into account small strain damping (Phillips & Hashash, 2009),

- Numerical scheme damping (e.g., Newmark, HHT), which can be used to introduce high-frequency damping on the numerical simulation.

In the last decades it has been generally agreed in scientific community and codes that EQL ground response analysis can be applied up to strains of around 0.1% (ASN/GUIDE/2/01 (Gupta & Lacoste, 2006)). Indeed, large maximum shear strains lead to (i) higher damping which may overdamp the moderate-to-high frequency content of the seismic signals in the surface and (ii) larger volumetric strains and pore-pressure build-up, which are not accounted for in standard EQL procedure.

Recent works from (Kaklamanos et al 2013) and (Kim, et al., 2016) pushed the analysis of the validity domain of standard EQL approach by comparing predictions both against large accelerometric databases and nonlinear model predictions. They have shown that indeed 0.1% seems to be the lower boundary of EQL acceptance rather the upper boundary, as a transition zone between EQL and nonlinear models up to around 0.4%-0.5% of maximum shear strains is obtained from the analysis.

More recently, EQL has been adopted to introduce site response in hazard accepting shear strains up to 0.5% (USNRC RIL2021-15, 2021, (Rodriguez-Marek, et al., 2021)). They justify the extension of EQL for higher strain levels beyond 0.1% based on research studies arguing that the latter have shown EQL analysis to be not sufficiently different from total stress nonlinear models for strains up to about 0.5% (e.g., (Kaklamanos, Baise, Thompson, & Dorfmann, 2015; Zalachoris & Rathje, 2015)). Likewise, ASCE 4-14 sets limitations for EQL analysis in the strain range 0.5%-1%. In Pecker et al 2017 a limit based on the reference strain is discussed.

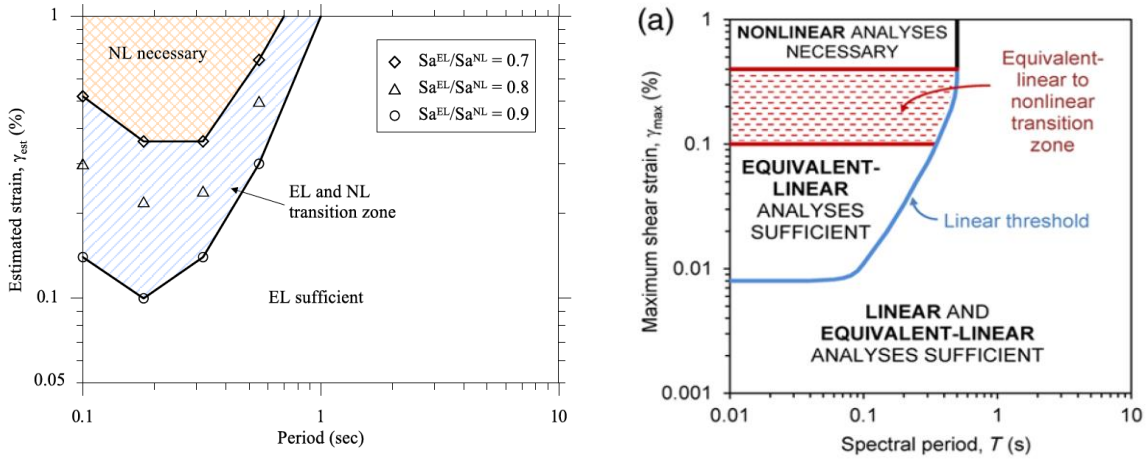

Kim et al., 2016 Kaklamanos et al., 2013

Figure 6: Domains of validity of EQL approach as proposed in literature by different authors.

Regarding nonlinear models, validity domain analysis of total stress regarding effective stress models based on large databases has not yet been conducted, as laboratory data usually available in such databases are insufficient to correctly calibrate effective stress models.

3.3. Uncertainty quantification and propagation in 1D equivalent linear site response

We adopt the classical workflow for the definition of the probabilistic analysis chain described in the **figure 7** below. The steps are 1) definition of the deterministic model and analysis, 2) identification of sources of uncertainty and quantification and 3) uncertainty propagation and statistical analysis and post-processing of the output.

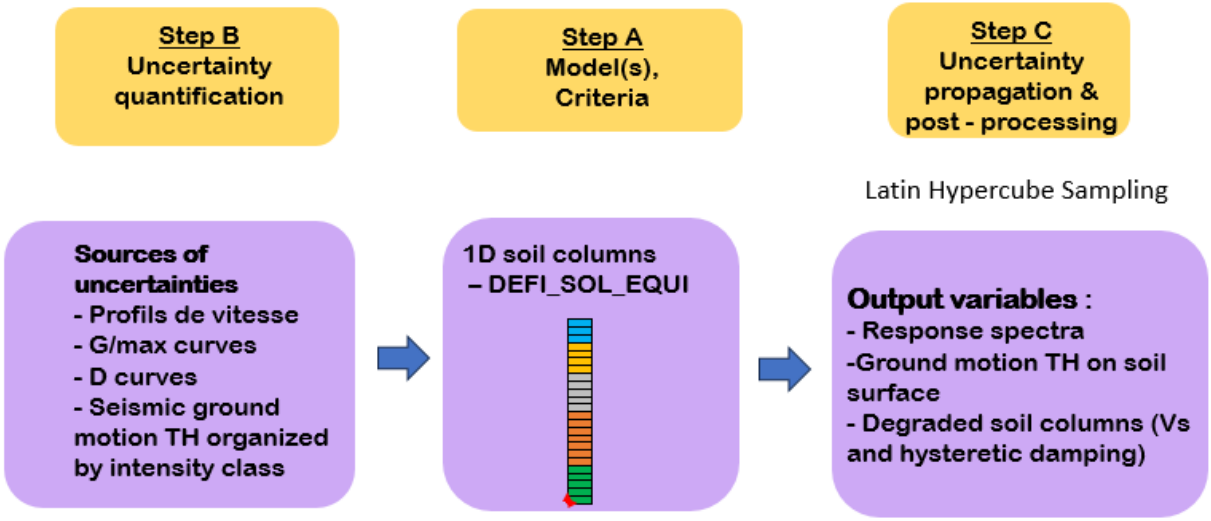

Figure 7 Overall view of the uncertainty analysis with the 3 steps: model definition, uncertainty quantification & propagation and post-processing of probabilistic results.

The output quantities of interest are here the ground motion TH on soil surface, the response spectra as well as the strain dependent properties of the soil columns (shear wave velocity Vs and hysteretic damping). These output quantities are in agreement with the needs for SSI studies performed in the framework of WP6. Note that for standard EQL procedure each horizontal TH leads to strain dependent soil properties (possibly different for the two horizontal directions), whereas 2-component approaches allow for obtaining one set of strain dependent soil properties per considered seismic event.

The main sources of uncertainty in the 1D site response analysis are the soil properties, material behaviour and the stratification characteristics (layer heights). Here, we consider in addition the variability of the seismic ground motion that introduces additional variability in the results.

In addition, the spatial variability of soil properties within a layer is sometimes accounted for by random field representations (El Haber, 2018; de la Torre, Bradley, & McGann, 2021; Youssef, 2023).

The impact of the different sources of uncertainty on the output quantities need to be assessed to optimise the model. The (Toro G. R., 1995; Toro G. R., 2022) model has been initially developed for cases with no or very few information on the local stratification and material properties which is why it introduces very high uncertainty and variability. Here we rather introduce a generic and comprehensive approach for the quantification of uncertainties in structural analysis as illustrated in the **Figure 7**.

The approach for uncertainty propagation presented here generalizes the methods proposed in the past for an application to arbitrary number of correlated random variables and distributions. Furthermore, we introduce the Latin Hypercube sampling LHS in order to improve convergence and reduce the required sample size.

3.3.1. Uncertainty quantification

In what follows we give an overview over the sources of uncertainty and probabilistic models to introduce these in 1D site response. We also give some elements on the parameterization of these probabilistic models based on literature and engineering design practice, in particular when limited site specific data is available. When abundant data is available then this should be used to determine required properties.

- **Soil Vs profiles**

A lognormal distribution is generally assumed for the Vs values. Recent studies confirmed appropriateness of this assumption e.g. (Youssef, 2023). In addition, the uncertainty of the layer heights can be accounted for. However, generally, the impact of layer heights uncertainty has only moderate impact on the results.

The best-estimate value of the Vs values for each layer is associated to the median of the lognormal random variable. The log standard deviation needs to be evaluated from site investigations. The variability of the soil Vs-values is to be understood as a local site variability including epistemic uncertainty related to experimental assessments but also natural variability of the soil profiles on the considered site.

If no site-specific information on this variability is available, then generic values must be adopted. In particular, the log-standard deviation (log-std) can be chosen in agreement with deterministic code criteria for defining intervals to be considered for the modulus G. For example, the log-std σ can be defined such that the interval (1/2, 2) corresponds to the ($\pm 2\sigma$) values or equivalently the 2.3%-97.7% fractiles of the random variable. Associating the interval (1/2, 2) the 2.3%-97.7% confidence intervals of the distribution yields $\beta_G = 0.35$ and thus $\beta_{Vs} = 0.175$.

Table 2 below compares this value to the ones obtained under different assumption on the deterministic intervals and corresponding fractiles of the probability distribution. Under high uncertainty, the (0.5, 2) intervals are preferred, these bounds are recommended as deterministic intervals in ASCE 4-14 for considering soil uncertainty in SSI. In any case these generic values can generally be reduced when detailed site investigations are available.

For comparison, in USNRC RIL2021-15 (2021) β_{Vs} = 0.15 has been retained which is slightly lower than what is assumed here. The latter value is in agreement with the findings of Toro (1995) for 3 site specific analysis reported in PEER 2014-16 by Steward et al (2014). The authors identified β_{Vs} = 0.15 for the first 50m for sites spaced by less than 800m. The same author identified generic β_{Vs} comprised between 0.27 and 0.37 for non site-specific data, that is generic data from sites with several kilometres distance.

The correlation introduced in the random sampling of the soil Vs profiles depends on the vicinity of the layers, i.e. adjacent layers have higher Vs correlation than distant ones.

Table 2: Dispersion of the Vs values for different deterministic intervals and corresponding fractiles of the probability distributions.

Deterministic intervals for the modulus G	0.5, 2	0.5, 2	2/3, 3/2	2/3, 3/2
Fractiles of the probability distribution for G	5%-95%	2.3%-97.7% ($\pm 2\sigma$)	5%-95%	2.3%-97.7% ($\pm 2\sigma$)
β_{Vs}	0.208	0.175	0.123	0.102

- **Modulus reduction curves**

We adopt a Gaussian distribution for G/Gmax. This is more in agreement with the nature of the considered variable (modulus reduction curve) and the available information on the dispersion from (Darendeli, 2001). The curves are truncated to not exceed 1 and to not take values below the reduction identified for 0.5% shear strain. In the linear equivalent analysis framework, it would not be physically sound to exceed the initial G value nor to accept null shear modulus.

The mean (which is here equal to the median) is taken as equal to best-estimate value while the standard deviation is taken from literature (Darendeli, 2001) . The generic and specific standard deviation values for Clay and sand gravel are given in **Figure 8**

- **Damping curves**

We adopt a lognormal distribution for shear strain dependant damping. This agrees with the physical nature of the variable (only positive values). The median of the distribution is equal to the best estimate value while the log-std is taken from literature (Darendeli, 2001) . The generic and specific standard deviation values for Clay and sand gravel are given in **Figure 8**.

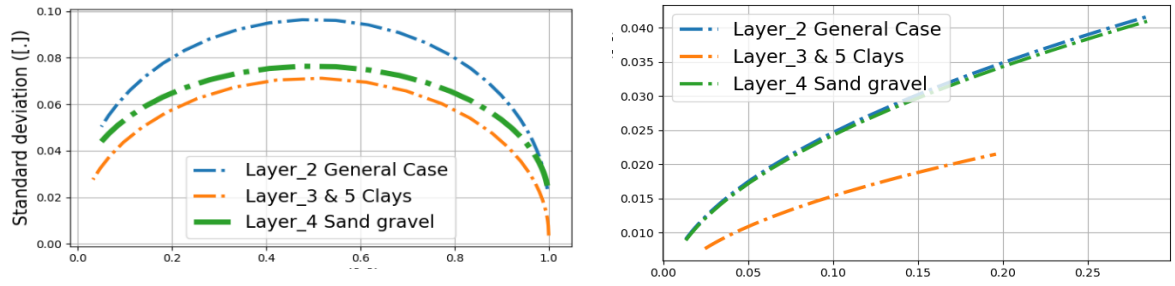

Figure 8: Generic and specific soil class standard deviation from (Darendeli, 2001), layer numbers refer to METIS case study.

- **Correlation structure**

The correlation between the D and G/Gmax values has to be considered as well as Vs correlation of neighboring soil layers. A negative correlation is generally introduced for G/Gmax and D curves with ρ=-0.5.

- **Small scale heterogeneities of soil properties within each layer**

It is generally acknowledged that soil exhibits small scale variability within each layer. This variability, as illustrated in **Figure 9**, can be modelled by random fields to represent the material heterogeneities (El Haber, 2018; Youssef, 2023).

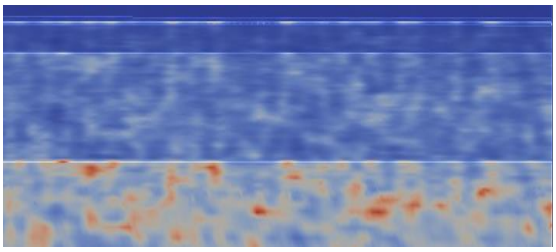

Figure 9: Illustration of modelling small-scale Vs variability within soil layers by random fields

3.3.2. Sampling of the correlated random variables

Algorithm

The algorithm used for the generation of correlated random variables using the Latin Hypercube Sampling (LHS) is as follows:

- Create a sampling of a vector of independent Gaussian random variables using the LHS.
- Construct the covariance matrix **C** and Cholesky decomposition and obtain correlated Gaussian random vector.
- Obtain correlated lognormal random vector by probability transformation.

To obtain the best fitting sample for a given sample size, the sampling procedure is repeated several times and the best sample (in terms of mean, std and correlation coefficient) is retained. This approach is applied to both the sampling of soil columns and the modulus reduction and damping curves.

Sample size

Currently 30 analyses are practice for uncertainty propagation in SSI while more analysis are carried out to propagate soil uncertainty in the site response analysis. Then the information on the soil uncertainty is summarized in a probability distribution and sampling of soil profiles for SSI is performed on this basis (30 samples) and the sampled soil columns are paired arbitrarily with the set of ground motion.

It is our goal here to implement an integrated approach where the soil columns from the site response analysis, paired to their corresponding ground motion, are directly used for SSI computations. In consequence, special has to be brought to the sample size since it has direct impact on the number of SSI analysis to be conducted.

In our example applications we identified a sample size of N=100 to well represent soil uncertainty but this has to be assessed for more examples to deduce general conclusions.

The **Figure 10** shows an example of soil profile generated with this procedure along with the convergence of estimations of the mean and std per layer.

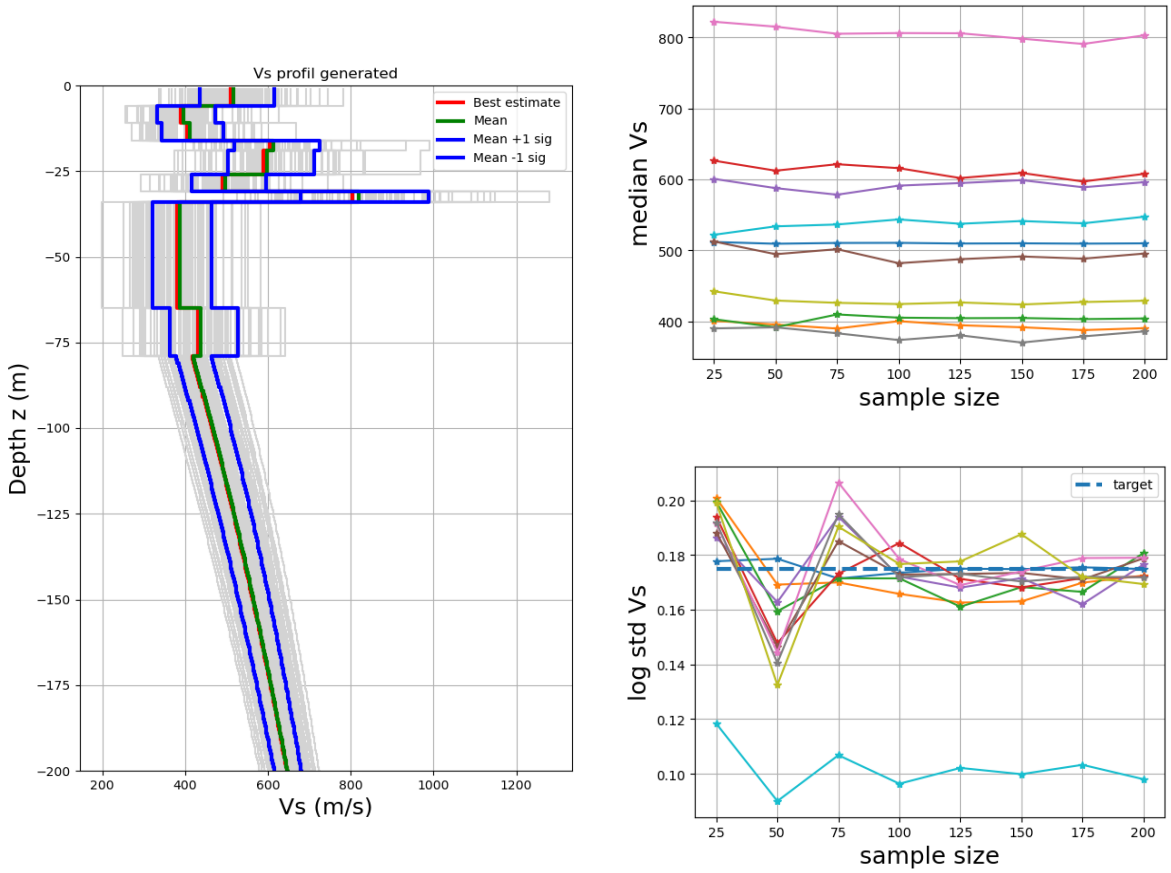

Figure 10: Example of a set of N=100 probabilistic soil columns and convergence of median and log-std as a function of N

The presented approach for uncertainty propagation builds on recent state of the art, such as (Stewart, Afshari, & Hashash, 2014; Bahrampouri, Rodriguez-Marek, Shahi, & Dawood, 2020) and constitutes an improved mathematical framework for uncertainty propagation. Sensitivity analyses are performed to rank the different sources of uncertainty and focus on the variables that have the largest impact on the results. This procedure is implemented in METIS based on python and code_aster and applied on METIS case-study (D5.4).

4. 2D/3D site response and spatial variability of the seismic ground motion

For far field seismic excitation and a quasi-horizontally stratified soil domain, the 1D site response analysis is recognized as a powerful tool as the 1D vertical plane wave propagation hypothesis remains valid for this scenario. Nevertheless, this hypothesis meets its limitations for more complex site conditions, such as 2D/3D basin amplification effects (Bard & Bouchon, 1980; Chavez-Garcia & Faccioli, 2000; Faccioli & Vanini, 2003; Poursartip & Kallivokas 2018; Touhami et al 2021) or near-field scenarios where directivity effect or multidimensional (2D/3D) site effects influence the spatial variability of the ground motion (GM) and thus cancelling the vertical plane wave propagation hypothesis (Abell, Orbović, McCallen, & Jeremić, 2018). To address such complex site conditions, more dimensional models possibly including the source need to be developed. The last part of this work focuses on numerical modelling

of 2D/3D site response and the consideration of the spatial variability of earthquake ground motion (GM) in a dynamic finite element (FEM) analysis.

Considering the uncertainties and the physical complexity of the seismic excitation and the soil domain, as well as computational constraints, several researchers (Herrera & Bielak, 1977; Bielak & Christiano, 1984; Léger & Boughoufalah, 1989; Zienkiewicz, Bicanic, & Shen, 1989; Wolf, 1989) proposed to define the incident wave field as an input at the boundary of the numerical model as the free-field ground motion excitation coming from an earthquake source.

In this context, two different strategies (**Figure 11**) can be defined for the definition of the input ground motion on the finite element analysis depending on the level of knowledge as well as the complexity of the wavefield for the site-specific application:

- **Vertical incidence plane wave excitation and the Free-Field Boundary Condition (FFBC):** The simplest and most common assumption for the ground motion definition is the plane wave excitation of vertical incidence. The ground motion of reference can be defined in a form of an acceleration time history at bedrock, either directly from a PSHA analysis (selection/generation of accelerograms, in correspondence with the strategy developed on the METIS project), or from a physics-based simulation. In this case, vertically polarized plane waves are considered for the base of the model, along with the FFBC (Zienkiewicz, Bicanic, & Shen, 1989; Wolf, 1989) on the lateral boundaries of the domain.
- **3D ground motion excitation and the Domain Reduction Method (DRM) approach:** A more advanced 3D boundary condition that allows the consideration of the spatial variability of the ground motion as an input to the numerical model, was initially introduced by (Bielak, Yoshimura, Hisada, & Fernández, 2003) as the Domain Reduction Method (DRM) approach. It consists of a two-steps weak coupling approach where the complete 3D wave field obtained from a source-to-site auxiliary domain simulation is replaced by equivalent nodal forces to be exerted on the boundary surface of a reduced domain, providing a realistic 3D definition of the seismic excitation. In practise, the advantage of the DRM approach lies in the fact that each step of the simulation can be solved separately with an appropriate numerical tool and based on the limitations of each problem. The spectral element method (SEM) couped to finite element method (FEM) as implemented in (Korres, et al., 2022) is presented here.

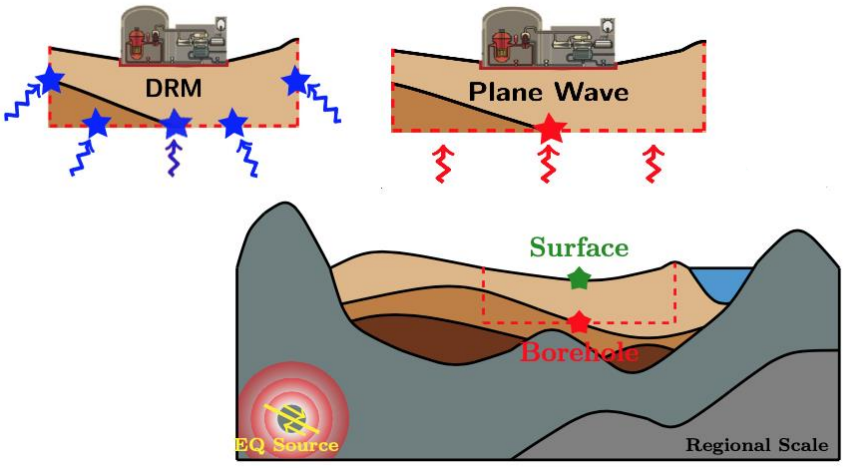

Figure 11: Proposed strategies for the analysis of multidimensional site-effects in a FEM framework with code aster.

Both strategies, are implemented in code aster and will be discussed in the following sub-sections. Nevertheless, it is worth mentioning that their correct implementation lies in the use of paraxial elements, an absorbing boundary condition implemented in code based on the work of (Modaressi & Benzenati, 1994). For reasons of completion, a brief description of the paraxial element formulation is

provided before moving on to the description of the two strategies for multidimensional site-effect analysis.

The following section is organised as follows: **Sub-section 4.1** provides a brief description of the paraxial element formulation to better understand the important parameters needed for the definition of the input motion excitation. **Sub-section 4.2** focuses on the simplified free-field boundary conditions. The methodology is presented for 2D and 3D applications, and an illustration of the importance of the FFBC is provided for a simplified 2D linear elastic soil profile. In **sub-section 4.3**, the regional scale simulation in SEM and the SEM-FEM coupling are presented for a realistic case study. In the last part of **sub-section 4.3**, a more recent implementation of the coupling is discussed based on a parallel version of the coupling. It shows the acceleration of the last part of the numerical analysis with FEM, allowing to move towards larger domains for the numerical analysis of multidimensional site-effects with code aster.

4.1. Paraxial elements as an absorbing boundary condition in code aster

Numerical simulation of wave propagation in a FEM framework, postulates the use of absorbing boundary conditions imposed on the boundary of the finite domain in order to absorb the outgoing waves and avoid unrealistic spurious reflections in the domain of interest. Different types of absorbing boundary conditions have been proposed in the literature over the last decades presenting different advantages and difficulties based on the application of interest: simple dashpot approach (Lysmer & Kuhlemeyer, 1969), damping layers (Semblat, Lenti, & Gandomzadeh, 2011; McCallen, et al., 2020), perfectly-matched layers (PML) (Berenger, 1994) *etc.*.

In the following and for all numerical studies to be performed with code aster, paraxial elements are used as an absorbing boundary condition. Paraxial elements are boundary conditions capable to both impose the dynamic excitation, as well as to absorb the outgoing waves arriving on the fictitious surface boundary (Modaressi & Benzenati, 1994). They were initially introduced by (Engquist & Majda, 1977) and (Clayton & Enquist, 1977), while the implemented version in Code_Aster is based on a modification initially discussed by (Modaressi & Benzenati, 1994) allowing to take into account the dynamic excitation.

4.1.1. Definition of the spectral impedance of the boundary Γ

Assume a finite domain of interest with a boundary Γ where the absorbing boundary condition is to be applied along with the seismic excitation (**Figure 12)**.

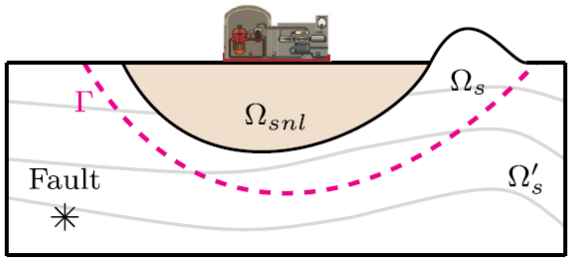

Figure 12: Schematic illustration of the problem.

Starting from the general expression of the elastic equation of motion, the derivation of the spectral impedance on the boundary of the reduced domain Γ requires the projection of the equation of motion on a local tangent plane $(\boldsymbol{e_1}, \boldsymbol{e_2})$, with outward normal $\boldsymbol{e_3}$. The solution of this projected equation, expressed in the Fourier wave number-frequency domain, $\hat{u}'$ and $\hat{u}_3$, leads to the derivation of the spectral impedance on the interface Γ, provided schematically with **Eq. 4.1**.

$$\hat{\boldsymbol{t}}(\boldsymbol{\xi}, \boldsymbol{x_3} = 0, \omega) = a_0 \boldsymbol{e_3} + b_0 \boldsymbol{\xi} + c_0 \boldsymbol{\xi} \times \boldsymbol{e_3} \quad (\mathbf{4.1})$$

Where a_0, b_0 and c_0 are functions of the wave number vector $\boldsymbol{\xi}$ associated with the local plane coordinate $\boldsymbol{x}'$ and the pulsation ω. To obtain the previous expression in the physical domain, an inverse Fourier transform must be applied, leading to:

$$\hat{\boldsymbol{t}}(x', \boldsymbol{x_3} = 0, t) = \int_{-\infty}^{+\infty} \int_{-\infty}^{+\infty} \hat{\boldsymbol{t}}(\boldsymbol{\xi}, \boldsymbol{x_3} = 0, \omega)\, e^{-i(\omega t + \xi x')} d\omega d\xi \quad (\mathbf{4.2})$$

4.1.2. Paraxial approximation of the impedance

The computation of the double integral in the last expression cannot be conveniently obtained for the general case of a complex geological domain and 3D excitation. To simplify this (Clayton & Enquist, 1977; Engquist & Majda, 1977) proposed to develop the wave numbers for the transverse ξ_S and longitudinal wave ξ_P as a function of the ratio κ.

$$\xi_P = \frac{\omega}{C_P}\sqrt{1 - C_P^2\kappa^2} \qquad \xi_S = \frac{\omega}{C_S}\sqrt{1 - C_S^2\kappa^2} \qquad where\ \kappa = \frac{|\xi|}{\omega} \quad (\mathbf{4.3})$$

where C_S and C_P are the shear and longitudinal wave velocities, respectively, under the assumption of linear isotropic elasticity. The wave vectors ξ_S and ξ_P can now be approximated through a Taylor expansion in the form of:

$$\xi_a = \frac{\omega}{C_a}\sqrt{1 - C_a^2\kappa^2} = \frac{\omega}{C_a}\left[1 - \frac{1}{2}C_a^2\kappa^2 + \cdots\right] \quad a = S, P \quad (\mathbf{4.4})$$

The paraxial approximation of the impedance consists in assuming that the ratio κ is sufficiently small ($\kappa \ll 1$), and thus the lower orders of the Taylor expansion are enough for the approximation of the values of ξ_S and ξ_P.

It is important to state here that this assumption of $\kappa \ll 1$ is valid for large frequencies ω or small ξ (propagation in the direction close to $\boldsymbol{e_3}$). More precisely, the wave vectors ξ_S and ξ_P take imaginary values (evanescent waves) for $|C_S\kappa| > 1$, and thus stability problems appear in the solution. An easy modification that allows to eliminate the evanescent component of the solution is based on the restriction of the range of solutions to those waves that propagate within a cone of the $\boldsymbol{e_3}$ vector (paraxial waves).

Here, the zero-order paraxial approximation is used in Code Aster (Electricité de France, 2017). Consequently, the expression of the spectral impedance (**Eq. 4.4**) can be rewritten in the schematic form of **Eq. 4.5,** which can be assimilated to a distribution of linear viscous dashpots:

$$\hat{\boldsymbol{t}}(\boldsymbol{\xi}, \boldsymbol{x_3} = 0, \omega) = A_0(\boldsymbol{\partial_t u}) \quad (\mathbf{4.5})$$

Where A_0 is a function of C_S and C_P.

It is worth noticing that the accuracy of the paraxial approximation could diminish significantly due to soil material heterogeneity, the increased wave-field complexity, and the angle of incidence of the arriving scattered wave field among others. Consequently, it is clear that when a more complex diffracted wave field with an angle of incidence far from the vertical one (*e.g.* surface waves, wave scattering) arrives on the boundary, the zero-order approximation present low absorbing performance (Clayton & Enquist, 1977; Engquist & Majda, 1977). This phenomenon might impact the size of the finite domain to be numerically modelled for the SSI problem and is discussed in (Korres, et al., 2022).

4.1.3. Variational formulation

In order to provide the expression of the external dynamic excitation the variational formulation of the problem is derived here. On the boundary surface Γ (**Figure 12**), a continuity of the displacement and traction vector needs to be considered to ensure the equilibrium on the interface (**Eq. 4.6**)

$$\begin{matrix} \boldsymbol{u_S} - \boldsymbol{u'_S} = \boldsymbol{0} \\ \boldsymbol{t_S} + \boldsymbol{t'_S}(\boldsymbol{u'_s}) = \boldsymbol{0} \end{matrix} \quad (4.6)$$

Based on the *Sommerfeld* radiation condition, the incident wave field $\boldsymbol{u'_i}$ has to be equal to the total wave field $\boldsymbol{u'_S}$ in infinity. Consequently, the diffracted wave field $\boldsymbol{u_r}$ can be expressed following **Eq. 4.7**

$$\begin{matrix} \boldsymbol{u'_S} = \boldsymbol{u'_i} + \boldsymbol{u'_r} \\ \lim_{r\to\infty} \|\boldsymbol{u'_r}\| = \boldsymbol{0} \end{matrix} \quad (4.7)$$

The diffracted field $\boldsymbol{u'_r}$ can now be completely described via the zero-order paraxial approximation and as a result the traction vector takes the following form:

$$\begin{matrix} \boldsymbol{t_S} = -\boldsymbol{t'_S}(\boldsymbol{u'_s}) = -\boldsymbol{t'_S}(\boldsymbol{u'_i}) - \boldsymbol{t'_S}(\boldsymbol{u'_r}) \approx -\boldsymbol{t'_S}(\boldsymbol{u'_i}) - A_0(\partial_t \boldsymbol{u'_r}) \Rightarrow \\ \boldsymbol{t_S} \approx -\boldsymbol{t'_S}(\boldsymbol{u'_i}) - A_0(\partial_t \boldsymbol{u'_s}) + A_0(\partial_t \boldsymbol{u'_i}) \end{matrix} \quad (4.8)$$

Finally, the variational formulation of the system can be expressed based on the expression of the traction vector:

$$\int_{\Omega_s} \rho \partial_{tt} \boldsymbol{u'_s} \cdot \boldsymbol{w} d\Omega + \int_{\Omega_s} \sigma'_s : (\boldsymbol{w}) d\Omega + \int_{\Gamma} A_0(\partial_t \boldsymbol{u'_s}) \cdot \boldsymbol{w}\, d\Gamma = \int_{\Gamma} \left(-\boldsymbol{t'_S}(\boldsymbol{u'_i}) + A_0(\partial_t \boldsymbol{u'_i})\right) \cdot \boldsymbol{w}\, d\Gamma \quad (4.9)$$

External forces representing the dynamic excitation are described from the right-hand side of **Eq. 4.9** from where it is clear that in order to define the excitation on the boundary of the finite domain, only the traction vector $\boldsymbol{t'_s}(\boldsymbol{u'_i})$, and the viscous stress vector field from the incident velocity field $A_0(\partial_t \boldsymbol{u'_i})$ are required. This conclusion is of crucial importance as it demonstrates which are the necessary fields to be defined on the boundary of the finite element domain for a correct definition of the dynamic excitation.

4.2. Bedrock PSHA output and the Free-Field Boundary Condition (FFBC) with a vertical incidence plane wave excitation

This section provides the key ideas of the construction of the free-field boundary condition in code aster. The FFBC approach as it was proposed by (Zienkiewicz, Bicanic, & Shen, 1989; Wolf, 1989), is discussed in the first part. At first for the simple 2D case before extending the approach for a 3D finite element analysis. An illustration of the importance of the FFBC is presented at the end of this part for 2D horizontally stratified soil domain.

4.2.1. The Free-Field Boundary Condition (FFBC)

It is most common in practical applications that information concerning the seismicity of the region of interest are constrained to a PSHA analysis performed for the bedrock of reference, while information concerning the form of the complete wave field is quite scarce. In accordance with PSHA analysis on bedrock, a multidimensional site-effect analysis can be performed by defining on the boundaries of the computational domain a plane wave excitation with vertical incidence. This plane wave is generally applied at the bottom of the computational domain, while the motion along the lateral sides in not known beforehand. A simple solution proposed by (Zienkiewicz, Bicanic, & Shen, 1989; Wolf, 1989), is the so-called free-field boundary condition (FFBC) where the excitation imposed on the lateral sides is the one obtained from the propagation in a 1D soil column as schematically represented in **Figure 13**.

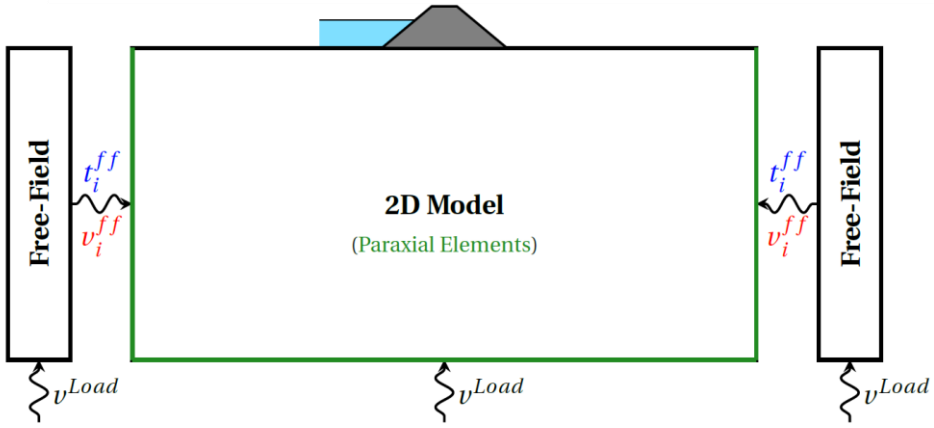

Figure 13: Schematic representation of the free-field boundary condition (FFBC).

The definition of the dynamic excitation in code aster is ensured via the use of paraxial elements as previously mentioned in **sub-section 4.1**. In this context, and based on **Eq. 4.9,** only the traction vector $\boldsymbol{t}_s'(\boldsymbol{u}_i')$ and the incident wave velocity field $\dot{\boldsymbol{u}}_i'$, are the necessary fields needed to correctly construct the FF excitation on the lateral boundary.

It is worth noticing that the 1D columns can be solved *à priori* in order to construct the dynamic excitation which is then transferred to the lateral boundary for the 2D dynamic analysis. This implies that no interaction takes place between the 1D column and the 2D profile as information is transferred unidirectionally from the 1D column to the 2D domain. This implies that the wave field generated in the 2D does not affect the free-field ground motion of the 1D propagation, a bold assumption that might be quite unrealistic depending on the complexity of the 2D analysis. Nevertheless, it can be justified in certain cases if the columns are placed at some distance from the central region of the model.

Finally, an extension of the FFBC can be done for the consideration of 3D site-effect analysis. This extension implies the *à priori* definition of the free-field ground motion on the lateral boundaries of the 3D domain. A schematic representation of the 1D-2D-3D approach is presented in **Figure 14** and the procedure of field transfer is executed as follows:

1. 1D propagation model: Define a 3D soil column with a unitary thickness in each corner of the 3D soil domain and solve the 1D propagation. Periodic boundary conditions are applied in the column.
2. 2D propagation model: Define the 2D slice with a unitary thickness in each side of the 3D model. Impose the plane wave excitation at the bottom of the model and the FF excitation coming from the solution of the 1D propagation model to the lateral boundaries of the 2D slice.
3. 3D propagation model: The 3D soil domain is considered, and the plane wave excitation is imposed at the base. The FFBC imposed on the lateral boundaries comes from the 2D propagation model.

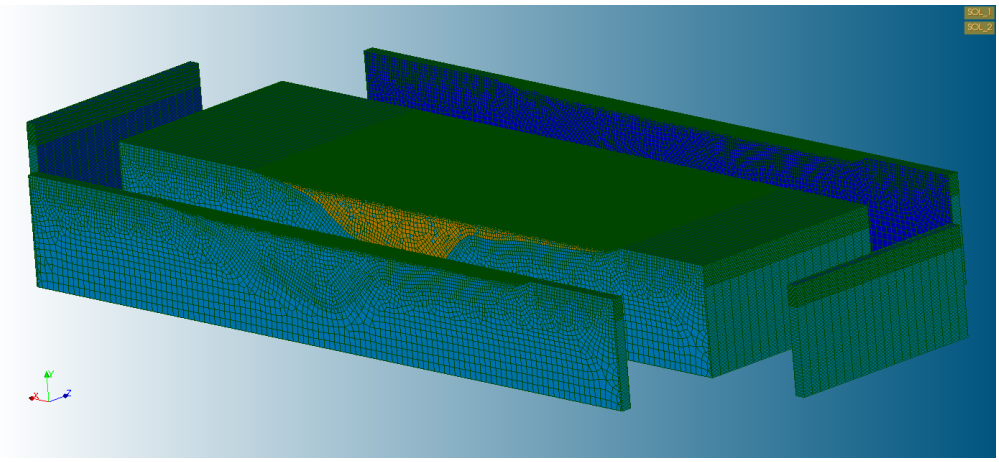

Figure 14: Free-field boundary condition for a 3D site-effects analysis.

4.2.2. Application for a simplified 2D soil domain

For illustration purposes, an application of the FFBC is performed on a simplified 2D soil profile. **Figure 15** presents the geometry and the mechanical properties of the 3 soil layers. Material behavior is supposed linear elastic for all three layers. Dynamic excitation is imposed at the base of the domain as a plane wave excitation with vertical incidence and paraxial elements are imposed at the base as well as at the lateral sides of the 2D profile.

Horizon	E [MPa]	ν [-]	ρ [kPa]
Couche 1	791	0.3	1970
Couche 2	783	0.3	1970
Couche 3	997	0.3	2070

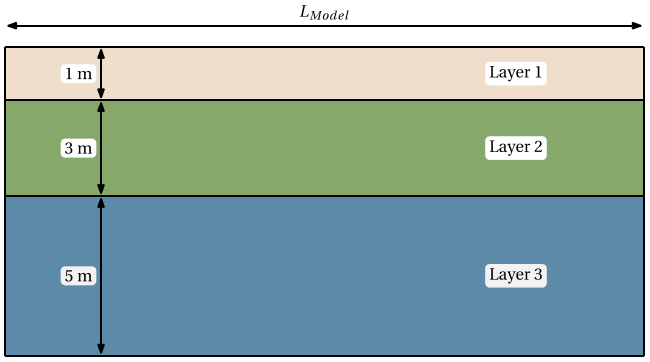

Figure 15: Mechanical properties (left) and geometry (right) of the 2D soil profile (Note that *couche* in the right figure means layer).

To evaluate the efficiency of the FFBC, three different numerical solutions are compared in this case study as shown in **Figure 16**:

- **Large/Small Model**: Excitation at the bottom, and paraxial elements imposed at the lateral sides of each model.
- **Small +FFBC**: Excitation at the bottom, and free-field boundary condition obtained from a previous analysis with a 1D soil column, imposed at the lateral sides of the small model.

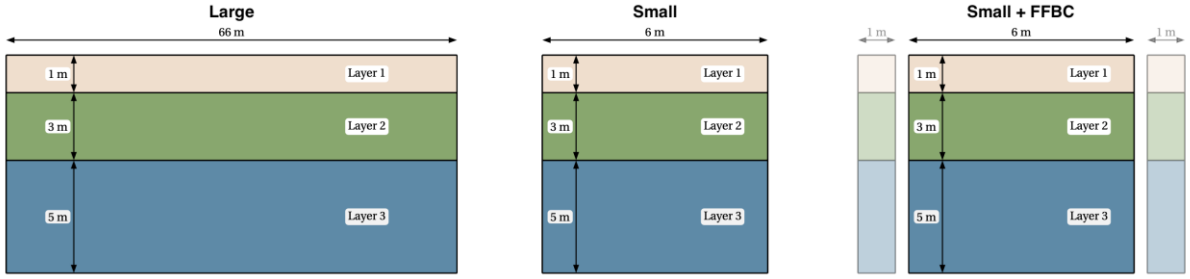

Figure 16: Geometry of the different solutions used to examine the efficiency of the FFBC in code aster.

Dynamic response of these three models, is compared with the free-field response obtained from a 1D wave propagation with a 1D soil column profile, used here as a solution of reference. Comparison of numerical results is performed in terms of acceleration time histories for a point located at the surface and the centre of each 2D profile. Numerical results are presented in **Figure 17**, where the solution of each numerical model (dashed red line) is compared to the solution of reference of the 1D soil column (black solid line). Main observations are summarized as follows:

- **Large model** (left in **Figure 17**): good representation of the solution of reference. Nevertheless, a lateral dimension of 66m is necessary to correctly model the free-field response.
- **Small model** (centre in **Figure 17**): poor representation of the free-field response due to the inefficient small size of the model (6 m compared to 66 m) and the presence of absorbing boundary conditions without FFBC. Periodic conditions need to be used in this case, such as applied to the 1D soil column (no structure is modelled in this example).
- **Small model + FFBC** (right in **Figure 17)**: excellent representation of the free-field solution. Even with the small domain size of 6 m, it can be observed that with the application of the FFBC on the lateral sides of the model the response at the surface is identical to the one obtained with the 1D soil column.

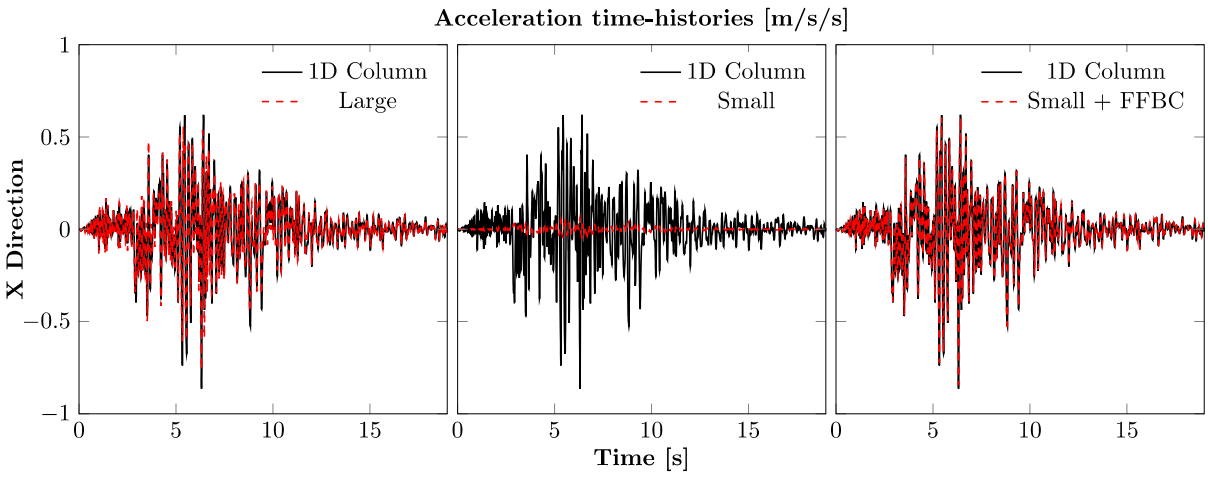

Figure 17: Comparison of the acceleration time histories at the surface of the soil domain.

In addition to acceleration time histories, numerical results are also compared using the criteria of (Kristeková, Kristek, Moczo, & Day, 2006) (Kristeková, Kristek, & Moczo, 2009). The criteria adopt a time-frequency representation (TFR) of the seismic signal, which is obtained after a continuous wavelet transformation. In this context, the evolution of the frequency content of the signal with respect to time can be easily represented and thus local time-frequency differences can be identified. Based on the aforementioned, a single value goodness-of-fit (GOF) criterion can be defined for the envelope and the phase of the signals to be compared. This single value GOF criterion will be used here to evaluate the solution obtained between the different models. The comparison is between a signal of reference (1D soil column) and a simulated solution (one of the respective models). The obtained score is in the scale

of 0 to 10 allowing to evaluate the similarity of the two signals: (i) for a value of 0 there is no correspondence between the two signals while for a value of 10 a perfect correspondence can be observed. Comparison points are placed along the different models as presented in **Figure 18**.

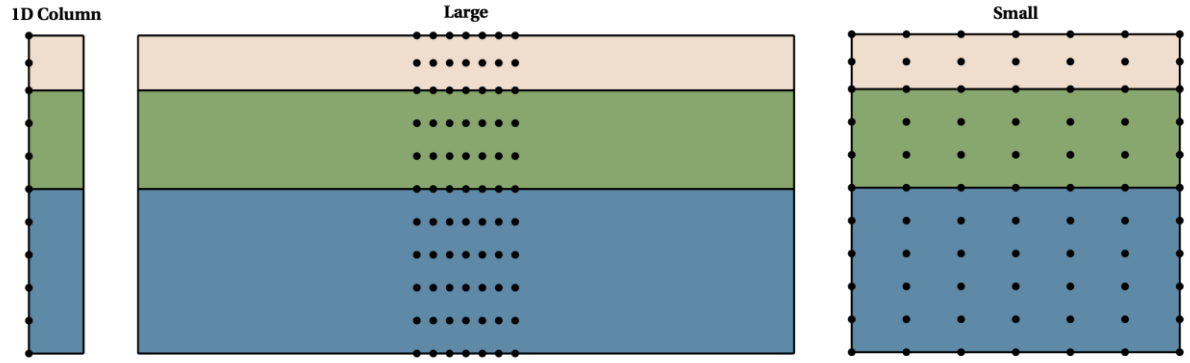

Figure 18: Points for the comparison based on the GoF score.

Numerical results based on the criteria of Kristeková and the GOF score are provided in **Figure 19**, for all three numerical solutions, along the X and Y coordinates of the model and with the colorbar representing the GOF score. Main observations are summarized as follows:

- **Large model** (left in **Figure 19**): a GOF≈ 8 signifying an almost excellent representation of the solution of reference along the complete domain.
- **Small model** (centre in **Figure 19**): poor representation of the free-field (GOF≈ 4). An increase of the score is observed towards the base of the model, where the dynamic excitation is imposed via the paraxial elements.
- **Small model + FFBC** (right in **Figure 179**): excellent representation of the free-field solution (GOF≈ 10).
-

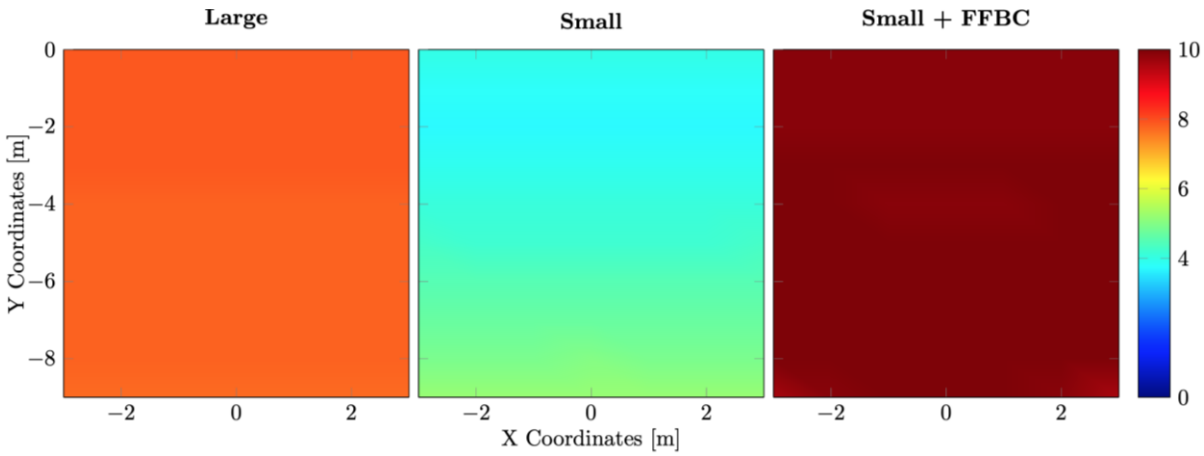

Figure 19: Evolution of the GOF score along the X-Y plane for each case study.

4.2.3. Partial Conclusions

The plane wave excitation with the FFBC was presented in this part for 2D and 3D site effect analysis in a FEM framework. This simplified boundary condition largely used in engineering applications (Ebrahimian, 2012; Karalar & Cavuslu, 2022) has several advantages mainly related to its simplicity and ease of implementation when it comes to practical application, as well as to its accordance to traditional PSHA outputs on outcropping bedrock. However, it is quite evident that the method quickly finds its limitations when it comes to more complex source excitation introducing directivity effects, and a spatial

variation of the earthquake ground motion. In these particular cases, a more realistic 3D input ground motion needs to be defined on the boundary of the numerical model allowing to take into account the aforementioned aspects. These aspects will be discussed in the next sub-section in the framework of the domain reduction method approach.

4.3. Regional scale simulation and the Domain Reduction Method approach

This section provides the key ideas of the coupling procedure. The DRM approach as it was proposed by (Bielak, Yoshimura, Hisada, & Fernández, 2003), is discussed in the first part. Then the specifics of the SEM-FEM coupling based on the chosen numerical tools are provided in the second and last part of this section. For a more detailed description of the specific SEM-FEM coupling between the two software code_aster and SEM3D, the reader should refer to (Korres, et al., 2022).

4.3.1. Domain Reduction Method (DRM)

The key concept of the DRM approach lies in the definition of a complex 3D incident wave field to be imposed as an input excitation to the reduced domain model (Bielak, Yoshimura, Hisada, & Fernández, 2003). In this framework, the objective of the DRM is to transfer the dynamic excitation of the seismic source closer to the boundaries of a reduced (smaller) domain of interest, at the scale of the site/structure.

For this purpose, source-to-structure wave propagation is considered in two separate steps, where the initial domain of interest Ω, is divided in two sub-domains by a virtual boundary surface Γ : i) the interior domain Ω_s , and ii) the exterior domain Ω_s' **(Figure 10**). The wave propagation problem is then solved in two separate steps:

- **Auxiliary domain problem** $\boldsymbol{P_0}$: Local features of interest (*e.g.* complex geology, structures, *etc.*) are replaced by a simpler soil profile in continuation of the soil in depth (see **Figure 10b**), and source-to-site propagation in the whole domain ($\Omega_s' \cup \Omega_s^0$) is performed in order to define the corresponding ground motion at the boundary (Γ) of an interior domain. Given the higher wave velocity of the soil a coarser mesh discretization can be chosen, leading to a faster source-to-site simulation.
- **Reduced domain problem** $\boldsymbol{P_r}$: The second step considers only the reduced ($\Omega_s \cup \Omega_{snl}$) domain and the local features of interest are explicitly accounted for (see **Figure 10**c). The input excitation expressed in terms of equivalent nodal forces obtained directly from $\boldsymbol{P_0}$ and applied on the so-called DRM boundary Γ in a region that is slightly bigger than the local reduced domain. The soil outside the boundary Γ is only used for absorbing the diffracted waves that travel out of the domain and are incompatible with $\boldsymbol{P_0}$ solution.

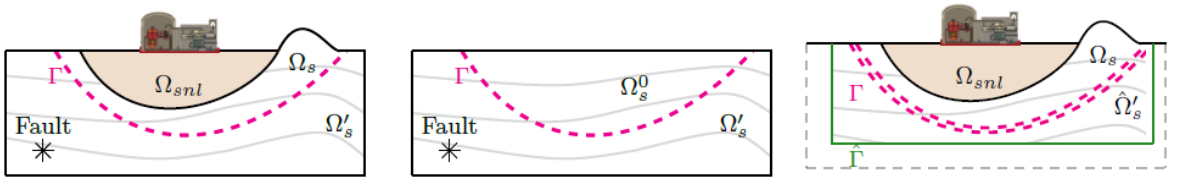

(a) Problem of reference. (b) Auxiliary domain problem. (c) Reduced domain problem.

Figure 10: Schematic representation of the domain reduction method (adopted from (Bielak, Yoshimura, Hisada, & Fernández, 2003))

Finally, it is important to remind here that in the DRM approach proposed by (Bielak, Yoshimura, Hisada, & Fernández, 2003), two key points must be treated: i) an external region with a suitable absorbing boundary condition around the reduced domain, and ii) the definition of the equivalent nodal forces on a region in the reduced domain boundary.

Concerning the former point, alternative approaches for suitable absorbing boundary conditions with the DRM methodology have been proposed in the literature: simple dash-pot approach (Yoshimura,

Bielak, Hisada, & Fernández, 2003; Preisig & Jeremic, 2005; Kontoe, Zdravkovic, & Potts, 2008; Petropoulos, 2008), among others, buffer zones or damping layers Bielak, Yoshimura, Hisada, & Fernández, 2003; Semblat, Lenti, & Gandomzadeh, 2011; Wang, Yang, Sinha, Luo, & Jeremic, 2017; Abell, Orbović, McCallen, & Jeremić, 2018; McCallen, et al., 2020), PML (Poursartip, Fathi, & Kallivokas, 2017; Poursartip & Kallivokas, 2018). In **section 4.1.2**, the adopted solution for the boundary condition (*i.e.* paraxial approximation) was presented.

As far as the latter point is concerned, a DRM interface needs to be defined for the computation of the equivalent nodal forces. The way that these equivalent nodal forces are computed and implemented in the current weak SEM-FEM coupling is presented in the following.

4.3.2. SEM-FEM Coupling description

As already demonstrated with **Eq. 4.9**, the traction vector $\boldsymbol{t}_s'(\boldsymbol{u}_i')$ and the incident wave velocity field $\dot{\boldsymbol{u}}_i'$, are the necessary fields in order to correctly construct the transient dynamic impedance with the paraxial elements on the boundary Γ of the reduced domain. Nevertheless, special care needs to be taken in the definition of this traction vector for each one of the numerical solutions.

Kinematic fields such as displacement and velocity, are discrete fields directly obtained as the solution of the numerical time integration scheme in each one of the two computational software. On the contrary, the traction vector, is obtained after a post-processing procedure, which is fundamentally different between SEM and FEM, due to their differences in terms of formulation (shape functions, quadrature rules and Degrees of Freedom - DoFs). In consequence, the approximation introduced from a direct transfer of a traction vector on the boundary of the reduced domain might lead to important errors in the definition of the dynamic excitation.

A remedy to this approximation, consists in reconstructing the traction vector on a FEM framework, based on the more accurate expression of the displacement fields directly obtained as the solution of the wave propagation problem in SEM3D.

Consequently, the necessary kinematic fields to be "transferred" between the two software are : i) the displacement field $\boldsymbol{u}$, exported in an auxiliary layer neighboring to the reduced domain boundary so as to reconstruct the traction vector in a FEM framework, and ii) the velocity field $\dot{\boldsymbol{u}}$ exported on the reduced domain boundary (**Figure 11**).

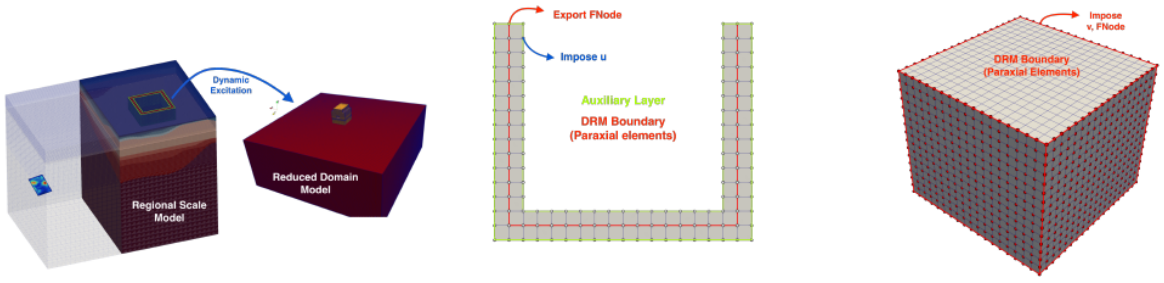

(a) Regional domain. (b) FEM Auxiliary layer. (c) Reduced domain.

Figure 11: Schematic representation of the coupling procedure between SEM3D and code_aster (reprinted from (Korres, et al., 2022))

A schematic representation of the coupling between SEM and FEM is presented in **Figure 11** and the procedure of field transfer is executed as follows:

1. Define the surface boundary of the DRM interface and the neighbouring auxiliary layer in SEM domain (**Figure 11**a).
2. Export displacement and velocity fields ($\boldsymbol{u}$, $\dot{\boldsymbol{u}}$) on predefined sensor points on Gauss-Lobatto-Legendre points lying on the DRM boundary and auxiliary layer. These points are the nodes of the FEM mesh, and the kinematic fields are obtained using the high order basis functions of

SEM. No spatial interpolation is therefore needed at this interface since a matching correspondence between SEM and FEM DoFs is enforced.

3. On the auxiliary layer (**Figure 11**b), impose nodal displacement field $\boldsymbol{u}$ and compute the traction vector solving the static problem with FEM. The traction vector defined on nodes is simply the nodal forces.

4. In the reduced domain (**Figure 11**c), reconstruct the dynamic excitation from using the velocity field $\dot{\boldsymbol{u}}$ directly exported from SEM, and the nodal forces F_{Node} computed in FEM from the auxiliary layer model.

All field transfer between the SEM and FEM codes was performed using MEDCoupling, an open-source SALOME[1] tool used for mesh/field handling (MEDCoupling, 2019).

It is important to state here that the proposed methodology for the computation of the traction vector assumes hexahedral 8-node linear elements within the FEM. One of the main advantages of the finite element method lies in the fact that quadratic elements as 10-node tetrahedral ones can be used in the numerical model to represent any more complex geometries as well as decrease the number of points per wavelength for a correct wave propagation. In this framework, the proposed methodology for the traction vector calculation must be adapted to a reduced domain discretized with quadratic tetrahedral elements between step 3 and 4 of the coupling procedure.

4.3.3. Regional scale simulation and coupling verification

The present analysis focuses on the region of the Niigata prefecture in Japan where is located the Kashiwazaki-Kariwa nuclear power plant (KKNPP) facility. The area of interest considered for the numerical model is represented in **Figure 12**, along with the location of the earthquake event, inspired by the 16/06/2007 aftershock - AS1 (in Figure 12a) registered in the region.

A $48 \times 48 \times 23\ km^3$ soil domain (auxiliary domain problem - $\boldsymbol{P_0}$) is numerically modelled in the spectral element code SEM3D, see for example (Touhami, Lopez-Caballero, & Clouteau, 2021) for more details, using 8×10^6 hexahedral spectral elements. Five Gauss Lobatto Legendre (GLL) points are used for each direction, leading to a model size of 8×10^9 degrees of freedom (DoFs). A representation of the mesh is provided in **Figure 12**b.

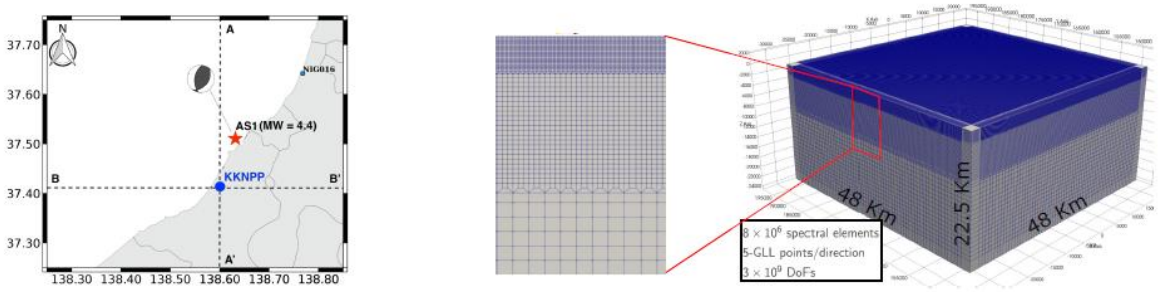

(a) Earthquake location. (b) Meshed soil domain.

Figure 12: Niigata region with borders of the SEM numerical model at the KKNPP site**.**

4.3.3.1. Regional 3D Geology

The geological profile used in this study consists of a complex regional geology model proposed by the Geological Survey of Japan (GSJ - (Sekiguchi, et al., 2009)). It is an improvement of the previous NIED (National Research Institute for Earth Science and Disaster Prevention) model proposed by (Fujiwara, Hirano, Abe, & Takizawa, 2006) for the Niigata area, based on several seismological observations.

[1] https://www.salome-platform.org/

A representation of the geological structure along the section AA' (**in Figure 12**a) is provided in **Figure 13**. The regional scale representation is given in the left figure (Figure 13a). In addition to this regional scale view of the geology, **Figure 13**b presents a closer look (white box in **Figure 13**a) at the region of the KKNPP facility in order to provide a better understanding of local geology. At the center of this "zoomed" version, the size of the FEM domain (reduced domain problem - $\boldsymbol{P_1}$) is provided. It is worth noticing, that the local scale FEM model ($520 \times 520 \times 190\, m^3$) is around 100 times smaller in each direction than the regional scale one, something that showcases the multi-scale character of the SEM-FEM coupling.

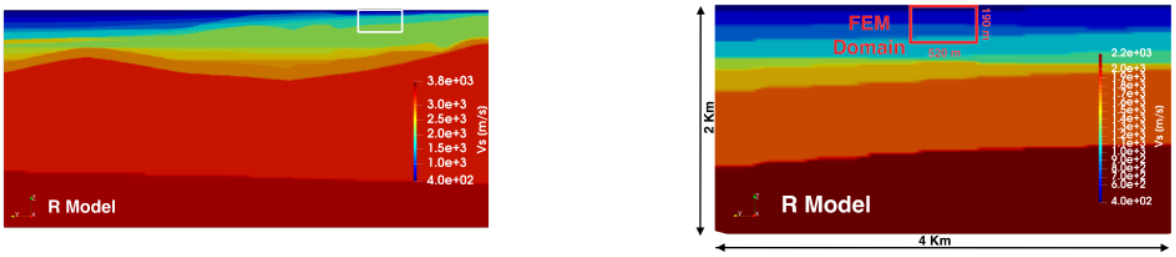

(a) Regional scale representation. (b) "Zoomed" version.

Figure 13: Shear wave velocity profile of the geological structure**.**

The corresponding mechanical linear isotropic characteristics of the FEM model of the reduced domain are provided in **Table** . Given the spatial variability of the mechanical properties, only the 1D profile along the Z direction and at the center of the reduced domain is given in this table. It is worth mentioning that in the current version of SEM3D there is no possibility to define a spatial variation of the attenuation parameters (Q_S, Q_P in **Table**). With this regard, a fixed value was chosen based on the mean value of the analysis presented in (Nakajima & Matsuzawa, 2017).

Table 3: 1D profile of mechanical parameters at the center of the FEM domain.

Depth [m]	ρ [kg/m3]	V_S [m/s]	V_P [m/s]	V_P/V_S [-]	Q_S [-]	Q_P [-]
-23	1990	400	1650	4.1	300	400
-55	2000	500	1750	3.5	-	-
-150	2050	600	1900	3.2	-	-
-190	2060	700	2010	2.9	-	-

Material layers definition in SEM3D is defined here using a not-honoring approach (see also (Touhami, Lopez-Caballero, & Clouteau, 2021)) which means that a predefined mesh grid can be used. With this regard, given the minimum shear wave velocity of $V_{Smin} = 400\, m/s$, the minimum element size of $L_{min} = 80\, m$ and the 5-GLL points per direction, the numerical model is expected to provide valid results for a maximum frequency of $f_{max} = \frac{400}{80} = 5\, Hz$. The SEM approximation being constructed based on high-order Lagrange polynomials and integrated with Gauss-Legendre-Lobatto quadrature rule, larger elements than FEM can be used for achieving the same maximum frequency than with the FEM. The maximum frequency value is however not sufficient for computing SSI and structural response where frequencies up to 30Hz or more need to be considered. In the future it is expected that the increase of computational capacities as well as advances in geophysical knowledge of seismic source and

propagation domains allows to considerably increase the maximum frequency. In addition, stochastic methods can be used to extend the results to higher frequencies, such approaches have however not been analysed in the current analysis but are under study.

4.3.3.2. Dynamic excitation and boundary conditions

The present analysis considers the aftershock AS1 event with a hypocenter located on the north part of the KKNPP site, as presented in **Figure 12**a. The aftershock event has a magnitude $M_{JMA} = 4.4$ (JMA stands for Japanese Meteorologic Agency), a hypocentral depth of 11 km, and a strike rake, and dip (ϕ, λ, δ) of 187^o, 70^o, and 54^o respectively.

Simulation of the fault rupture in SEM3D is performed here using the Ruiz Integral Kinematic (RIK) source model, as it was proposed by (Gallovič, 2016).

It consists of an advanced kinematic-fractal model accounting for the generation of broadband signals via the fault rupture simulation. Source rupture is simulated as a series of multiple sub-events and each sub-event is modelled using circles, the distribution of which, is based on a fractal distribution describing the number-size relation.

Given the size-number relation, the next step lies in the definition of the slip distribution considered in the source model. The distribution of the RIK sub-sources is constrained by a spatial probability density function with respect to a predefined normalized slip model and the total seismic moment defined for the seismic scenario. The slip model used to constrain the randomly generated slip for a new event can be obtained through an inversion process as in (Gallovič, 2016). Nevertheless, in this case, a slip model for an earthquake of similar magnitude ($M_{JMA} = 4.4$) and the seismic context in Japan was directly retrieved from the literature (Ide, 2001).

The parameters used to generate the source model as well as the generated slip distribution are provided in **Figure 14**. For a more detailed description concerning the RIK model and its configuration for the examined case, the reader should refer to (Korres, 2021).

Parameters	Values
Fault Dimensions	3.48 km × 3 km
Fault Discretisation	60 m × 60 m
Number of subsources	2900
Slip pulse width (L_0)	350 m
Rupture Velocity (V_R)	$0.8 \times V_S$

(a) Parameters of the source model.

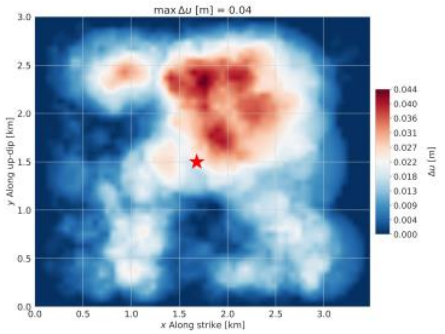

(b) Slip distribution.

Figure 14: Earthquake scenario based on the RIK model (reprinted by (Korres, et al., 2022))

Finally, Perfectly Matched Layers (PML) are used as absorbing boundary conditions in SEM3D to avoid spurious reflections on the boundaries.

4.3.3.3. Numerical Verification

The numerical verification of the presented SEM-FEM coupling is extensively discussed in (Korres, et al., 2022) and is not the main objective of the presented work. Nevertheless, for reasons of completion, the comparison of the acceleration time histories between a full-SEM3D propagation and a SEM/FEM

simulation and for several points at the surface of the reduced domain are provided in **Figure 15**. According to this **Figure 15**, an excellent correspondence is observed between the two approaches.

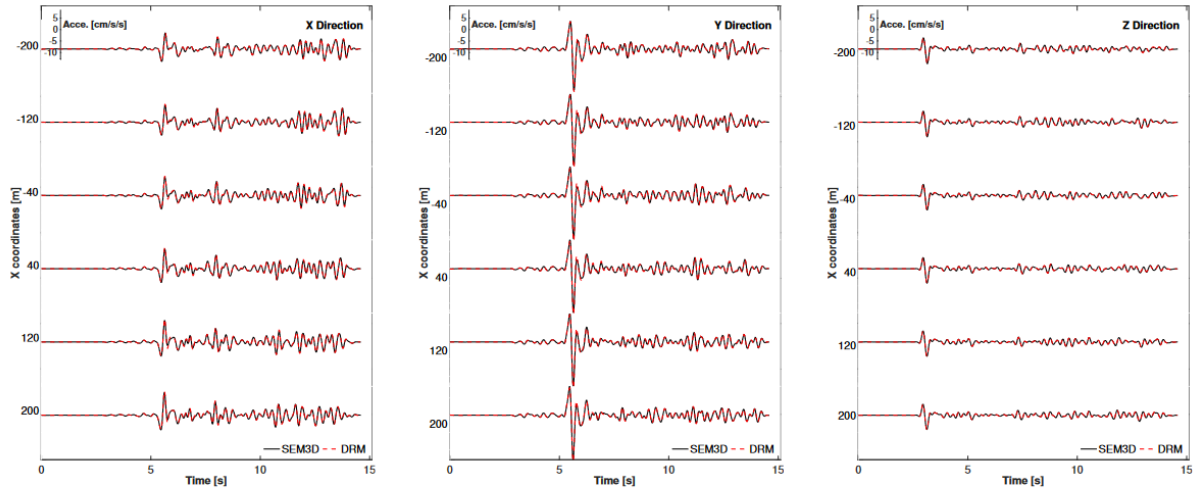

(a) X component. (b) Y component. (c) Z component.

Figure 15: Comparison of acceleration time histories at the surface of the reduced domain.

4.3.4. Towards a High-Performance Computing resolution with FEM

The case-study and the numerical verification of the coupling for the case of interest were presented in the previous part. Here, the analysis focuses on the second step of the DRM approach and the adaptation of the finite element problem in a High-Performance Computing (HPC) framework.

4.3.4.1. The initial implementation of the coupling

The initial implementation of the SEM-FEM coupling (Korres, et al., 2022) adopts the construction of the FEM model in a sequential sense, meaning that all the information concerning the discretized FEM domain, as well as the input excitation on the FEM boundary, is known by all MPI processes. Once the model is constructed, a parallel resolution of the dynamic system can be performed employing a direct parallel solver with *e.g.* MUMPS (Amestoy, Guermouche, L'Excellent, & Pralet, 2006), or parallel iterative solvers with PETSc (Balay, Abhyankar, Adams, Benson, & Brune, 2023). In other words, all the data are available on every process and only the elementary computations, assembly, and solution phases are done in parallel. This type of parallelism provides important advantages in terms of acceleration of the computational time highlighted in several engineering studies with code aster.

Nevertheless, the current approach does not allow to efficiently utilize computational resources and becomes unfeasible in cases where physical problems with larger domains in terms of DoFs need to be numerically simulated. Such examples are the SSI analysis of whole nuclear island buildings or the multi-dimensional site-effect analysis including 3D realistic basins in a FEM framework to allow a better representation of several physical phenomena.

4.3.4.2. The adaptation of the coupling in a domain decomposition framework

In order to optimize the usage of computational resources, the coupling procedure was entirely revisited and adapted in a domain decomposition framework (Tardieu, Alves Fernandes, & Devesa, 2019), where the whole domain is partitioned into several overlapping sub-domains and each sub-domain is processed separately by a MPI process. This partition includes the mesh of the reduced domain, as well as the input excitation field that needs to be defined on the boundary. As a result, each MPI process only knows information about the domain that is attributed to. Communications between sub-domains ensure the consistency of data on the overlapping "ghost layer" (Fan, Nihei, Myer, Cook, & Rector, 1997), where the exchange of information takes place between the traditional MPI communication process.

An example of the decomposition of the previous problem for 5 MPI processes is provided in **Figure 16**. The partition of the mesh is given in **Figure 16**a and each colored sub-domain is attributed to one MPI process. In a similar way, the partitioned input field (coming from the SEM3D simulation) is provided in **Figure 16**b. It is worth noticing that, the partitioning of the input field, corresponds to the partitioning of the whole meshed domain. It can be seen through the presence of the one element overlapping "ghost layer" where the exchange of information takes place between the traditional MPI communication process in **Figure 16**b.

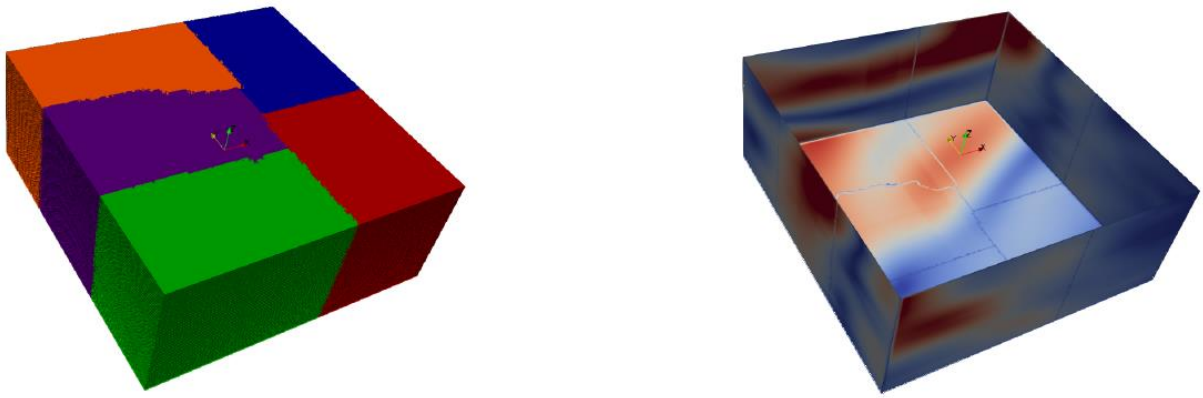

(a) Mesh partition. (b) Input field partition.

Figure 16: An example of the domain decomposition of the problem for 5 MPI processes.

4.3.4.3. Comparison between the different approaches

For illustration purposes, a comparison is provided here between different approaches to showcase the numerical performance of the HPC adaptation for the coupling. Three different cases are compared in this framework:

- **Sequential solution**: It consists of the initial version of the coupling in a sequential mode with 1 MPI process.
- **Parallel direct solver**: It consists of the initial version of the coupling and a parallel direct solver using MUMPS (Amestoy, Guermouche, L'Excellent, & Pralet, 2006) for the dynamic resolution of the problem.
- **HPC resolution**: Solution based on the domain decomposition approach using iterative solvers based on PETSc (Balay, Abhyankar, Adams, Benson, & Brune, 2023). The pre-conditioner used in this case is a simple precision factorization using MUMPS (Amestoy, Guermouche, L'Excellent, & Pralet, 2006).

The FEM soil domain examined in the coupling verification is considered here for the comparison procedure. It is represented using 2×10^6 degrees of freedom, a size that allows an easy solution even for the sequential case.

Numerical performance is provided with **Figure 17** where the evolution of the computational time (CPU Time) is presented with respect to the number of the MPI processes considered for the solution of the dynamic problem**.** In **Figure 17**, the purple dot corresponds to the sequential solution (2M DoFs for 1 MPI process), the red line corresponds to the parallel direct solver and the black line to the HPC resolution. The blue dots stand for the computation with 80 MPI processes, corresponding to 25K DoFs per MPI process.

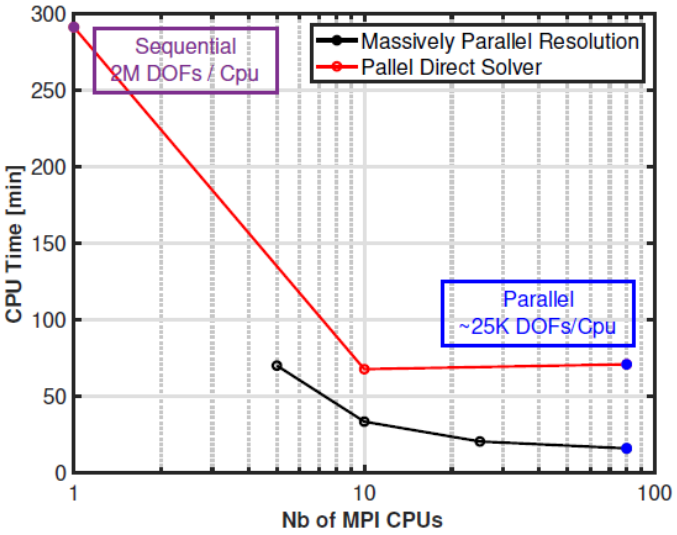

Figure 17: Evolution of the resolution CPU Time with respect to the number of MPI processes**.**

Main conclusions deriving from this **Figure 17** can be summarized as follows:

- The MUMPS direct parallel solver for 80 MPI processes takes around 1 h of CPU Time, which is $\times 5$ faster than the sequential solution. A "stagnation" of the CPU time is observed in this case as no important gains in CPU time can be observed between the solution with 10 MPI processes ($\approx 200 \times 10^3$ DoFs / MPI) and the one with 80 MPI processes ($\approx 25 \times 10^3$DoFs / MPI). This can be justified from the saturation of the attributed memory for the numerical resolution.
- The HPC resolution for the same number of 80 MPI processes takes around 15 min, which is $\times 4$ faster than the parallel direct solver, and $\times 20$ faster than the sequential solution.
- A saturation of the CPU time is observed for the HPC resolution after 10 MPI processes. This can be explained from the fact that the size of the problem remains small and thus for a larger number of MPI processes the ratio of DoFs/MPI remains small.

5.Conclusion

In this document, we report and summarize different approaches for the conduction of site response analysis depending on the configurations of the site. In particular, we introduce a set of indicators that can be used to assess whether 1D or multidimensional site response analysis should be developed. Then we present approaches to develop 1D or multidimensional site response. While the 1D site response analysis has been widely studied and applied in literature, including for nuclear safety applications, the 2D and in particular 3D site response analysis are still challenging in terms of modelling, data and computational resources. Regarding the 1D site response, comprehensive frameworks for uncertainty propagation and the consideration of nonlinearity in the framework of EQL analysis or nonlinear analysis are feasible. The approach is fully compatible with the analysis chain where SSI is computed based on time histories on soil surface associated to soil columns.

Regarding multidimensional site response analysis and in particular 3D models, it is expected that knowledge increases due to experimental campaigns and the further exploitation of new and existing seismological data (including knowledge about faults and thus extended seismic sources). Still, there is the need to account for uncertainty given the imperfect knowledge of source and propagation medium It is clear that efficient methods for uncertainty quantification and propagation are crucial elements in the deployment of such approaches. We are aware of. The introduction of 3D site response analysis into seismic safety analysis and in particular the development of a framework in agreement with current

approaches for the definition of seismic hazard and thus load based on PSHA results still needs to be set up.

Two strategies of increasing complexity were discussed in this work to tackle the multi-dimensional (2D and 3D site effects) analysis in a FEM framework:

- **The plane wave excitation with the Free-Field Boundary Condition (FFBC) in a FEM framework:** This simplified boundary condition largely used in engineering applications (Ebrahimian, 2012; Karalar & Cavuslu, 2022) has several advantages mainly related to its simplicity and ease of implementation when it comes to practical application, as well as to its accordance to traditional PSHA outputs on outcropping bedrock. However, the method cannot account for more complex near field and extended source excitation introducing directivity effects, and a spatial variation of the earthquake ground motion. In these particular cases, a more realistic 3D input ground motion needs to be defined on the boundary of the numerical model allowing to take into account the aforementioned aspects.
- **The domain reduction method (DRM) approach for the definition of a complex 3D input motion at the boundaries of the FE model:** The 3D ground motion is defined here using a SEM-FEM weak coupling for the source-to-site wave propagation. A brief verification of the coupling for the case-study of the Niigata region in Japan was presented at the first part. Then the analysis focuses on the adaptation of the FEM solution in a massively parallel framework, presenting the important advantages of the newly implemented approach. In overall, the main conclusions can be summarized as follows:
    - Optimization of the usage of numerical resources in terms of memory demands: Each MPI processor knows only information on mesh and field of sub-domain, and as a result memory demands are lower per MPI processor.
    - Scalability of numerical performance to the available computational resources.
    - Faster resolution of "traditional/trivial" problems compared to direct solver approaches. This stems mainly from the optimized manipulation of computational resources.
    - Possibility to handle larger domains in terms of DoFs in a FEM framework.

The HPC resolution approach presents some important advantages, nevertheless some "caution" key points also need to be taken into consideration:

- Numerical performance depends on the efficiency of the data exchange between the two software. In this framework, further validation needs to be performed for larger problems.
- Numerical performance also depends on the pre-conditioner as not all pre-conditioners are adapted for the same type of physical simulation.
- Particular conditions, such as Lagrange multipliers also play a crucial role as they significantly reduce the performance of iterative solvers.

The approaches discussed here have been assessed and evaluated for different example applications described in this report. Simplified methodologies and guidelines to define the input motion for DRM approach compatible with regulatory definitions of design motions have yet to be set up.

The application to METIS case study will be reported in the upcoming deliverable D5.4.

6. Bibliography

Abell, J. A., Orbović, N., McCallen, D. B., & Jeremić, B. (2018, February). Earthquake soil-structure interaction of nuclear power plants, differences in response to 3-D, 3 1-D, and 1-D excitations. *Earthquake Engineering and Structural Dynamics*. doi:10.1002/eqe.3026

Alshembari, R., Parolai, S., Boxberger, T., Sandron, D., Pilz, M., & Sylacheva, N. (2019, November). Seasonality in Site Response: An Example from Two Historical Earthquakes in Kazakhstan. *Seismological Research Letters, 91*, 415–426. doi:https://doi.org/10.1785/0220190114

Amestoy, P., Guermouche, A., L'Excellent, J.-Y., & Pralet, S. (2006, 2). Hybrid scheduling for the parallel solution of linear systems. *Parallel Computing, 32*(2), 136-156.

Anderson, J. G., & Hough, S. E. (1984). A model for the shape of the Fourier amplitude spectrum of acceleration at high frequencies. *Bulletin of the Seismological Society of America, 74*, 1969–1993.

ASCE Standard 4-14, Seismic analysis of safety-related nuclear structures

ASN/GUIDE/2/01 (2006), Prise en compte du risque sismique à la conception des ouvrages de génie civil d'installations nucléaires de base à l'exception des 2600.

Bahrampouri, M., Rodriguez-Marek, A., & Bommer, J. J. (2019, November). Mapping the uncertainty in modulus reduction and damping curves onto the uncertainty of site amplification functions. *Soil Dynamics and Earthquake Engineering, 126*, 105091. doi:https://doi.org/10.1016/j.soildyn.2018.02.022

Bahrampouri, M., Rodriguez-Marek, A., Shahi, S., & Dawood, H. (2020, September). An updated database for ground motion parameters for KiK-net records. *Earthquake Spectra, 37*, 505–522. doi:https://doi.org/10.1177/8755293020952447

Balay, S., Abhyankar, S., Adams, M., Benson, S., & Brune, J. B. (2023). PETSc Web page. Retrieved from https://petsc.org/

Bard, P.-Y., & Bouchon, M. (1980, 8). The seismic response of sediment-filled valleys. Part 1. The case of incident SH waves. *Bulletin of the Seismological Society of America, 70*(4), 1263-1286.

Barnaba, C., Marello, L., Vuan, A., Palmieri, F., Romanelli, M., Priolo, E., & Braitenberg, C. (2010, February). The buried shape of an alpine valley from gravity surveys, seismic and ambient noise analysis. *Geophysical Journal International, 180*, 715–733. doi:https://doi.org/10.1111/j.1365-246X.2009.04428.x

Berenger, J.-P. (1994, 10). A perfectly matched layer for the absorption of electromagnetic waves. *Journal of Computational Physics, 114*(2), 185-200.

Berge-Thierry, C., Svay, A., Laurendeau, A., Chartier, T., Perron, V., Guyonnet-Benaize, C., . . . Theodoulidis, N. (2017, November). Toward an integrated seismic risk assessment for nuclear safety improving current French methodologies through the SINAPS@ research project. *Nuclear Engineering and Design, 323*, 185–201. doi:10.1016/j.nucengdes.2016.07.004

Bielak, J., & Christiano, P. (1984). On the effective seismic input for non-linear soil-structure interaction systems. *Earthquake engineering & structural dynamics, 12*(3), 107-119. Retrieved from http://onlinelibrary.wiley.com/doi/10.1002/eqe.4290120108/abstract

Bielak, J., Yoshimura, C., Hisada, Y., & Fernández, A. (2003). Domain Reduction Method for Three-Dimensional Earthquake Modeling in Localized Regions, Part I: Theory. *Bulletin of the Seismological Society of America, 93*, 825–840. doi:10.1785/0120010251

Brune, J. N. (1970). Tectonic stress and the spectra of seismic shear waves from earthquakes. *Journal of geophysical research, 75*, 4997–5009.

Cadet, H., P. Y. Bard, A. Rodriguez-Marek, 2012. Site effect assessment using KiK-net 503 data: Part 1. A simple correction procedure for surface/downhole spectral ratios. *Bulletin of the* 504 *Seismological Society of America*, 10, 421-448.

Chavez-Garcia, F., & Faccioli, E. (2000). Complex site effects and building codes: making the leap. *Journal of seismology, 4*, 23--40. doi:https://doi.org/10.1023/A:1009830201929

Cherubini S., Z. I. (2020). *Study of the variability of 1D site response in Kushiro10 from records and an analytical model. SIGMA2-2020-D4-048 Research and Development Program on Seismic Ground Motion.* Tech. rep. Retrieved from https://www.sigma-2.net/medias/files/sigma2-2020-d4-048-kushiro-cherubini-zentner-approved-public-.pdf

Clayton, R., & Enquist, B. (1977). Absorbing boundary conditions for acoustic and elastic wave equations. *Bulletin of the seismological society of America, 67*(6), 1529-1540.

Code_Aster. (2017). *General public licensed structural mechanics finite element software, included in the Salomé-Méca simulation platform. Website http://www.code-aster.org. En particulier : [R4.05.06] Méthode linéaire équivalent pour la propagation des ondes en 1D.* Tech. rep., Electricité de France. Retrieved from https://code-aster.org/V2/doc/default/fr/man_r/r4/r4.05.06.pdf

Cornou, C. (2003, December). Contribution of Dense Array Analysis to the Identification and Quantification of Basin-Edge-Induced Waves, Part II: Application to Grenoble Basin (French Alps). *Bulletin of the Seismological Society of America, 93*, 2624–2648. doi:https://doi.org/10.1785/0120020140

Darendeli, M. B. (2001). *Development of a new family of normalized modulus reduction and material damping curves.* Ph.D. dissertation, The university of Texas at Austin.

de la Torre, C. A., Bradley, B. A., & McGann, C. R. (2021, November). 2D Geotechnical site-response analysis including soil heterogeneity and wave scattering. *Earthquake Spectra, 38*, 1124–1147. doi:https://doi.org/10.1177/87552930211056667

Ebrahimian, B. (2012, 2). Non-Linear Numerical Analysis of Earthquake- Induced Deformation of Earth-Fill Dams. *Advances in Geotechnical Earthquake Engineering - Soil Liquefaction and Seismic Safety of Dams and Monuments*.

Edwards, B., Michel, C., Poggi, V., & Fah, D. (2013, July). Determination of Site Amplification from Regional Seismicity: Application to the Swiss National Seismic Networks. *Seismological Research Letters, 84*, 611–621. doi:https://doi.org/10.1785/0220120176

El Haber, E. (2018). *Effet de la variabilité spatiale des propriétés du sol sur la variabilité de la réponse sismique.* Ph.D. dissertation, Université Grenoble Alpes (ComUE).

Electricité de France. (2017). *General public licensed structural mechanics finite element software, included in the Salomé-Méca simulation platform. Website http://www.code-aster.org. En particulier : [R4.02.05] Éléments de frontière absorbante.*

Engquist, B., & Majda, A. (1977, 7). Absorbing Boundary Conditions for the Numerical Simulation of Waves. *Mathematics of Computation, 31*(139), 629.

Faccioli, E., & Vanini, M. (2003, 10). Complex seismic site effects in sediment-filled valleys and implications on design spectra. *Progress in Structural Engineering and Materials, 5*(4), 223-238.

Fan, J., Nihei, K., Myer, L., Cook, N., & Rector, J. (1997, 1). Overlap domain decomposition method for wave propagation. *SEG Technical Program Expanded Abstracts 1997*, 1485-1488.

Fujiwara, T., Hirano, N., Abe, N., & Takizawa, K. (2006, 3). Subsurface Structure of the "Petit-spot" Intra-plate Volcanism, in the Northwestern Pacific. *JAMSTEC Report of Research and Development, 3*(0), 31-42.

Gallovič, F. (2016). Modeling velocity recordings of the mw 6.0 south napa, California, earthquake: Unilateral event with weak high-frequency directivity. *Seismological Research Letters, 87*(1), 1-14.

Gardner, J. K., & Knopoff, L. (1974). Is the sequence of earthquakes in Southern California, with aftershocks removed, Poissonian? *Bulletin of the seismological society of America, 64*, 1363–1367.

Griffiths, S. C., Cox, B. R., Rathje, E. M., & Teague, D. P. (2016a). Mapping dispersion misfit and uncertainty in V s profiles to variability in site response estimates. Journal of Geotechnical and Geoenvironmental Engineering, 142(11), 04016062.

Griffiths, S. C., Cox, B. R., & Rathje, E. M. (2016b). Challenges associated with site response analyses for soft soils subjected to high-intensity input ground motions. Soil Dynamics and Earthquake Engineering, 85, 1-10.

Groholski, D. R., Hashash, Y. M., Kim, B., Musgrove, M., Harmon, J., & Stewart, J. P. (2016, September). Simplified Model for Small-Strain Nonlinearity and Strength in 1D Seismic Site Response Analysis. *Journal of Geotechnical and Geoenvironmental Engineering, 142*. doi:https://doi.org/10.1061/(ASCE)GT.1943-5606.0001496

Gupta, O., & Lacoste, A. C. (2006). Prise en compte du risque sismique à la conception des ouvrages de génie civil d'installations nucléaire de base à l'exception des stockages à long terme des déchets radioactifs. Guide de l'Autorité de Sûreté Nucléaire. *Guide de l'Autorité de Sûreté Nucléaire*.

Hallo, M., Bergamo, P., & Fäh, D. (2022, June). Stochastic Model to Characterize High-Frequency Ground Motion at Depth Validated by KiK-Net Vertical Array Data. *Bulletin of the Seismological Society of America, 112*, 1997–2017. doi:https://doi.org/10.1785/0120220038

Herrera, I., & Bielak, J. (1977). Soil-structure interaction as a diffraction problem. *Proc. for 6th World Conference on Earthquake Engineering, 2*, 1467-1472.

Ide, S. (2001). Complex source processes and the interaction of moderate earthquakes during the earthquake swarm in the Hida-Mountains, Japan, 1998. *Tectonophysics, 334*(1), 35-54.

Idriss, I. M., Seed, H. B., Mechanics, C. U., & Laboratory, B. M. (1967). *Response of Horizontal Soil Layers During Earthquakes.* Department of Civil Engineering, University of California. Retrieved from https://books.google.fr/books?id=vXWvGAAACAAJ

Idriss, I. M., Sun, J. I., University of California, D. C., Building, & Division, F. R. (1992). *User's Manual for Shake91: A Computer Program for Conducting Equivalent Linear Seismic Response Analyses of Horizontally Layered Soil Deposits.* Center for Geotechnical Modeling, Department of Civil and Environmental Engineering, University of California, Davis. Retrieved from https://books.google.fr/books?id=3X01NQAACAAJ

Kaklamanos J., Bradley B. A., Thomspon E. M., and Baise L. G., (2013), Critical Parameters Affecting Bias and Variability in Site-Response Analyses Using KIK-net Downhole Array Data, Bulletin of the Seismological Society of America

Kaklamanos, J., Baise, L. G., Thompson, E. M., & Dorfmann, L. (2015). Comparison of 1D linear, equivalent-linear, and nonlinear site response models at six KiK-net validation sites. *Soil Dynamics and Earthquake Engineering, 69*, 207–219. doi:https://doi.org/10.1016/j.soildyn.2014.10.016

Kaklamanos, J., Bradley, B. A., Moolacattu, A. N., & Picard, B. M. (2020, March). Physical Hypotheses for Adjusting Coarse Profiles and Improving 1D Site-Response Estimation Assessed at 10 KiK-net Sites. *Bulletin of the Seismological Society of America, 110*, 1338–1358. doi:https://doi.org/10.1785/0120190263

Karalar, M., & Cavuslu, M. (2022, 12). Determination of 3D near fault seismic behaviour of Oroville earth fill dam using burger material model and free field-quiet boundary conditions. *Mathematical and Computer Modelling of Dynamical Systems, 28*(1), 55-77.

Kawase, H. (2006). Borehole observation for site effect studies. *Proc. of Third International Symposium on the Effects of Surface Geology on Seismic Motion, Grenoble, France, 30 August-1 September, invited, 2006*, (pp. 3–20).

Kawase, H., & Matsuo, H. (2004). Amplification characteristics of K-NET, KiK-net, and JMA Shindokei network sites based on the spectral inversion technique. *13th world conference on earthquake engineering.*

Kim, B., Hashash, Y. M., Stewart, J. P., Rathje, E. M., Harmon, J. A., Musgrove, M. I., . . . Silva, W. J. (2016, August). Relative Differences between Nonlinear and Equivalent-Linear 1-D Site Response Analyses. *Earthquake Spectra, 32*, 1845–1865. doi:https://doi.org/10.1193/051215EQS068M

Knopoff, L. (1964, February). A matrix method for elastic wave problems. *Bulletin of the Seismological Society of America, 54*, 431–438. doi:https://doi.org/10.1785/BSSA0540010431

Kontoe, S., Zdravkovic, L., & Potts, D. (2008). The domain reduction method for dynamic coupled consolidation problems in geotechnical engineering. *International journal for numerical and analytical methods in geomechanics, 32*, 659–680.

Korres, M. (2021). *Coupled 3D physics-based simulations for seismic source-to-structure response : Application to the Kashiwazaki-Kariwa nuclear power plant (Japan) case.* Ph.D. dissertation. Retrieved from http://www.theses.fr/2021UPAST118

Korres, M., Lopez-Caballero, F., Alves Fernandes, V., Gatti, F., Zentner, I., Voldoire, F., . . . Castro-Cruz, D. (2022). Enhanced seismic response prediction of critical structures via 3D regional scale physics-based earthquake simulation. *Journal of Earthquake Engineering*, 1–29.

Kristeková, M., Kristek, J., & Moczo, P. (2009). Time-frequency misfit and goodness-of-fit criteria for quantitative comparison of time signals. *Geophysical Journal International*, 813-825.

Kristeková, M., Kristek, J., Moczo, P., & Day, S. (2006). Misfit criteria for quantitative comparison of seismograms. *Bulletin of the seismological Society of America*, 1836-1850.

Kteich, Z., Labbé, P., Javelaud, E., Semblat, J.-F., & Bennabi, A. (2019, June). Extended equivalent linear model (X-ELM) to assess liquefaction triggering: Application to the City of Urayasu during the 2011 Tohoku earthquake. *Soils and Foundations, 59*, 750–763. doi:https://doi.org/10.1016/j.sandf.2019.02.002

Laurendeau, A., Bard, P.-Y., Hollender, F., Perron, V., Foundotos, L., Ktenidou, O.-J., & Hernandez, B. (2017, May). Derivation of consistent hard rock (1000 &lt\mathsemicolon{}{ }{VS} &lt\mathsemicolon{}{ }{3}000 m/s) GMPEs from surface and down-hole recordings: analysis of KiK-net data. *Bulletin of Earthquake Engineering, 16*, 2253–2284. doi:https://link.springer.com/article/10.1007/s10518-017-0142-6

Léger, P., & Boughoufalah, M. (1989, 1). Earthquake input mechanisms for time-domain analysis of dam—foundation systems. *Engineering Structures, 11*(1), 37-46. Retrieved from https://linkinghub.elsevier.com/retrieve/pii/014102968990031X

Li, W., & Assimaki, D. (2010, May). Site- and Motion-Dependent Parametric Uncertainty of Site-Response Analyses in Earthquake Simulations. *Bulletin of the Seismological Society of America, 100*, 954–968. doi:https://doi.org/10.1785/0120090030

Lin, J. (1991). Divergence measures based on the Shannon entropy. *IEEE Transactions on Information Theory, 37*, 145–151. doi:https://doi.org/10.1109/18.61115

Lysmer, J., & Kuhlemeyer, R. (1969, 8). Finite Dynamic Model for Infinite Media. *Journal of the Engineering Mechanics Division, 95*(4), 859-877.

Matsushima, S., Kosaka, H., & Kawase, H. (2017, July). Directionally dependent horizontal-to-vertical spectral ratios of microtremors at Onahama, Fukushima, Japan. *Earth, Planets and Space, 69*. doi:http://dx.doi.org/10.1186/s40623-017-0680-9

McCallen, D., Petersson, A., Rodgers, A., Pitarka, A., Miah, M., Petrone, F., . . . Tang, H. (2020). EQSIM—A multidisciplinary framework for fault-to-structure earthquake simulations on exascale computers part I: Computational models and workflow. *Earthquake Spectra*. doi:10.1177/8755293020970982

McCallen, D., Petrone, F., Miah, M., Pitarka, A., Rodgers, A., & Abrahamson, N. (2020). EQSIM—A multidisciplinary framework for fault-to-structure earthquake simulations on exascale computers, part II: Regional simulations of building response. *Earthquake Spectra*. doi:10.1177/8755293020970980

MEDCoupling. (2019). ``MEDCoupling developer's guide'', SALOME-platform, [Online] Available: http://docs.salome-platform.org/latest/dev/MEDCoupling/developer/index.html, [Accessed 17 04 2020]. ``*MEDCoupling developer's guide'', SALOME-platform, [Online] Available: http://docs.salome-platform.org/latest/dev/MEDCoupling/developer/index.html, [Accessed 17 04 2020]*. Retrieved April 17, 2020

Modaressi, H., & Benzenati, I. (1994). Paraxial approximation for poroelastic media. *Soil Dynamics and Earthquake Engineering, 13*(2), 117-129.

Nakajima, J., & Matsuzawa, T. (2017, 12). Anelastic properties beneath the Niigata–Kobe Tectonic Zone, Japan. *Earth, Planets and Space, 69*(1), 33.

Narayan, J. P., & Kumar, R. (2013, November). Spatial spectral amplification of basin-transduced Rayleigh waves. *Natural Hazards, 71*, 751–765. doi:10.1007/s11069-013-0917-2

Oth, A., Bindi, D., Parolai, S., & Giacomo, D. D. (2010, October). Earthquake scaling characteristics and the scale-(in)dependence of seismic energy-to-moment ratio: Insights from KiK-net data in Japan. *Geophysical Research Letters, 37*. doi:https://doi.org/10.1029/2010GL044572

Pagliaroli, A., Lanzo, G., Tommasi, P., & Fiore, V. D. (2013, April). Dynamic characterization of soils and soft rocks of the Central Archeological Area of Rome. *Bulletin of Earthquake Engineering, 12*, 1365–1381. doi:https://doi.org/10.1007/s10518-013-9452-5

Parolai, S., Bindi, D., & Pilz, M. (2015, January).: The role of Intrinsic and Scattering Attenuation. *Bulletin of the Seismological Society of America, 105*, 1049–1052. doi:https://doi.org/10.1785/0120140305

Passeri, F., Foti, S., & Rodriguez-Marek, A. (2020, September). A new geostatistical model for shear wave velocity profiles. *Soil Dynamics and Earthquake Engineering, 136*, 106247. doi:https://doi.org/10.1016/j.soildyn.2020.106247

Pecker, A. et al. (2017) An Overview of the SIGMA Research Project A European Approach to Seismic Hazard Analysis, ISBN 978-3-319-58153-8.

Petropoulos, G. (2008). *Soil-structure interaction analysis using high-performance parallel computation.* University of California, Berkeley.

Phillips, C., & Hashash, Y. M. (2009, July). Damping formulation for nonlinear 1D site response analyses. *Soil Dynamics and Earthquake Engineering, 29*, 1143–1158. doi:https://doi.org/10.1016/j.soildyn.2009.01.004

Pilz, M., & Cotton, F. (2019, May). Does the One-Dimensional Assumption Hold for Site Response Analysis? A Study of Seismic Site Responses and Implication for Ground Motion Assessment Using KiK-Net Strong-Motion Data. *Earthquake Spectra, 35*, 883–905. doi:https://doi.org/10.1193/050718EQS113M

Pilz, M., & Fäh, D. (2017, January). The contribution of scattering to near-surface attenuation. *Journal of Seismology, 21*, 837–855. doi:https://doi.org/10.1007/s10950-017-9638-4

Poursartip, B., & Kallivokas, L. F. (2018). Model dimensionality effects on the amplification of seismic waves. *Soil Dynamics and Earthquake Engineering, 113*, 572–592. doi:10.1016/j.soildyn.2018.06.012

Poursartip, B., Fathi, A., & Kallivokas, L. F. (2017). Seismic wave amplification by topographic features: A parametric study. *Soil Dynamics and Earthquake Engineering, 92*, 503-527. doi:https://doi.org/10.1016/j.soildyn.2016.10.031

Preisig, M., & Jeremic, B. (2005). *Nonlinear finite element analysis of dynamic soil-foundation-structure interaction.* Tech. rep., University of California, Davis.

Rathje, E. M., Kottke, A. R., & Trent, W. L. (2010, April). Influence of Input Motion and Site Property Variabilities on Seismic Site Response Analysis. *Journal of Geotechnical and Geoenvironmental Engineering, 136*, 607–619. doi:https://doi.org/10.1061/(ASCE)GT.1943-5606.0000255

Rodriguez-Marek A, Rathje E., Ake J, Munson C, Stovall S, weaver T, Ulmer K, and Juckett M (2021a), Documentation Report for SSHAC level 2: Site Response, Research Information Letter RIL 2021-15, ML21323A056, U.S. Nuclear Regulatory Commission

Rodriguez-Marek, R., Ozcebe, A., Smerzini, C., & Lai, C. (2021b). Aggravation factors for 2D site effects in sedimentary basins: The case of Norcia, central Italy. *Soil Dynamics and Earthquake Engineering, 149*, 106854.

Rodriguez-Marek, A., Rathje, E. M., Bommer, J. J., Scherbaum, F., & Stafford, P. J. (2014, June). Application of Single-Station Sigma and Site-Response Characterization in a Probabilistic Seismic-Hazard Analysis for a New Nuclear Site. *Bulletin of the Seismological Society of America, 104*, 1601–1619. doi:https://doi.org/10.1785/0120130196

Roten, D., Fäh, D., Cornou, C., & Giardini, D. (2006, June). Two-dimensional resonances in Alpine valleys identified from ambient vibration wavefields. *Geophysical Journal International, 165*, 889–905. doi:https://dx.doi.org/10.1111/j.1365-246X.2006.02935.x

Sekiguchi, H., Yoshimi, M., Horikawa, H., Yoshida, K., Suzuki, H., Matsuyama, H., . . . Ying, L. (2009). 3D subsurface structure model of the Niigata sedimentary basin. (9), 175-259.

Semblat, J.-F., Lenti, L., & Gandomzadeh, A. (2011). A simple multi-directional absorbing layer method to simulate elastic wave propagation in unbounded domains. *International Journal for Numerical Methods in Engineering, 85*, 1543-1563. doi:https://doi.org/10.1002/nme.3035

Shible, H., Hollender, F., Traversa, P., & Bard, P.-Y. (2023, June). Ground-Motion Model for Hard-Rock Sites by Correction of Surface Recordings (Part 1): Comparison of Site-Response Estimates at KiK-Net Sites. *Bulletin of the Seismological Society of America, 113*, 2164–2185. doi:https://doi.org/10.1785/0120220203

Spearman, C. (1904, April). "General Intelligence," Objectively Determined and Measured. *The American Journal of Psychology, 15*, 201. doi:https://doi.org/10.2307/1412107

Stewart, J. P., Afshari, K., & Hashash, Y. M. (2014). Guidelines for performing hazard-consistent one-dimensional ground response analysis for ground motion prediction. *PEER 2014-16.*

Tao, Y., & Rathje, E. (2019, July). Insights into Modeling Small-Strain Site Response Derived from Downhole Array Data. *Journal of Geotechnical and Geoenvironmental Engineering, 145*. doi:https://doi.org/10.1061/(ASCE)GT.1943-5606.0002048

Tao, Y., & Rathje, E. (2020, January). Taxonomy for evaluating the site-specific applicability of one-dimensional ground response analysis. *Soil Dynamics and Earthquake Engineering, 128*, 105865. doi:http://dx.doi.org/10.1016/j.soildyn.2019.105865

Tardieu, N., Alves Fernandes, V., & Devesa, G. (2019). Modélisation des effets de site multidimensionnels par le calcul haute-performance avec code_aster. *14ème Colloque National en Calcul de Structures*.

Teague, D. P., Cox, B. R., & Rathje, E. M. (2018). Measured vs. predicted site response at the Garner Valley Downhole Array considering shear wave velocity uncertainty from borehole and surface wave methods. Soil Dynamics and Earthquake Engineering, 113, 339-355.

Tchawe, F. N., Gelis, C., BONILLA, L. F., & Lopez-Caballero, F. (2021, April). Effects of 2-D random velocity perturbations on 2-D\less{}{i}{}\greater{}{SH}{}\less{}{/}{i}\greater{}{s}{h}ort-period ground motion simulations in the basin of Nice, France. *Geophysical Journal International, 226*, 847–861. doi:https://doi.org/10.1093/gji/ggab141

Thompson, E. M., Baise, L. G., Kayen, R. E., & Guzina, B. B. (2009, September). Impediments to Predicting Site Response: Seismic Property Estimation and Modeling Simplifications. *Bulletin of the Seismological Society of America, 99*, 2927–2949. doi:https://doi.org/10.1785/0120080224

Thompson, E. M., Baise, L. G., Tanaka, Y., & Kayen, R. E. (2012, October). A taxonomy of site response complexity. *Soil Dynamics and Earthquake Engineering, 41*, 32–43. doi:https://d1wqtxts1xzle7.cloudfront.net/53038139/dx.doi.org/10.1016/j.soildyn.2012.04.005

Toro, G. R. (1995). Probabilistic models of site velocity profiles for generic and site-specific ground-motion amplification studies. *Technical Rep, 779574*.

Toro, G. R. (2022, March). Uncertainty in Shear-Wave Velocity Profiles. *Journal of Seismology, 26*, 713–730. doi:https://doi.org/10.1007/s10950-022-10084-x

Touhami, S., Lopez-Caballero, F., & Clouteau, D. (2021, 2). A holistic approach of numerical analysis of the geology effects on ground motion prediction: Argostoli site test. *Journal of Seismology, 25*(1), 115-140.

Uebayashi, H. (2003, April). Extrapolation of Irregular Subsurface Structures Using the Horizontal-to-Vertical Spectral Ratio of Long-Period Microtremors. *Bulletin of the Seismological Society of America, 93*, 570–582. doi:https://doi.org/10.1785/0120020137

Uebayashi, H., Kawabe, H., & Kamae, K. (2012, March). Reproduction of microseism H/V spectral features using a three-dimensional complex topographical model of the sediment-bedrock interface in the Osaka sedimentary basin. *Geophysical Journal International, 189*, 1060–1074. doi:https://doi.org/10.1111/j.1365-246X.2012.05408.x

Wang, H., Yang, H., Sinha, S. K., Luo, C., & Jeremic, B. (2017). 3D non-linear earthquake soil-structure interaction modeling of embedded small modular reactor (SMR). *Proceedings of the 24th International Conference on Structural Mechanics in Reactor Technology (SMiRT 24)', Busan, South Korea.*

Wolf, J. (1989, 2). Soil-structure-interaction analysis in time domain. *Nuclear Engineering and Design, 111*(3), 381-393.

Yoshimura, C., Bielak, J., Hisada, Y., & Fernández, A. (2003). Domain reduction method for three-dimensional earthquake modeling in localized regions, part II: Verification and applications. *Bulletin of the seismological Society of America, 93*, 825–841.

Youssef, E. (2023). *Simulation of the seismic response in complex media: accounting for the soil spatial variability using non-stationary random fields and application to Beirut city (Lebanon).* Ph.D. dissertation, Université Grenoble Alpes et Université Libanaise.

Zalachoris, G., & Rathje, E. M. (2015, December). Evaluation of One-Dimensional Site Response Techniques Using Borehole Arrays. *Journal of Geotechnical and Geoenvironmental Engineering, 141*. doi:http://dx.doi.org/10.1061/(ASCE)GT.1943-5606.0001366

Zhu, C., Cotton, F., Kwak, D.-Y., Ji, K., Kawase, H., & Pilz, M. (2021, November). Within-site variability in earthquake site response. *Geophysical Journal International, 229*, 1268–1281. doi:https://doi.org/10.1093/gji/ggab481

Zienkiewicz, O., Bicanic, N., & Shen, F. (1989). Earthquake Input Definition and the Trasmitting Boundary Conditions. *Advances in computational nonlinear mechanics*, 109-138.